

A new coordinate-transformed discretization method for minimum entropy moment approximations of linear kinetic equations¹

Tobias Leibner^a, Mario Ohlberger^b

^a*Fachbereich Mathematik und Informatik, WWU Münster, Einsteinstrasse 62, 48149 Münster, tobias.leibner@uni-muenster.de*

^b*Fachbereich Mathematik und Informatik, WWU Münster, Einsteinstrasse 62, 48149 Münster, mario.ohlberger@uni-muenster.de*

Abstract

In this contribution we derive and analyze a new numerical method for kinetic equations based on a coordinate transformation of the moment approximation. Classical minimum-entropy moment (M_N) closures are a class of reduced models for kinetic equations that conserve many of the fundamental physical properties of the solutions. However, their practical use is limited by their high-computational cost, as an optimization problem has to be solved for every cell in the space-time grid. In addition, implementation of numerical solvers for these models is hampered by the fact that the optimization problems are only well-defined if the moment vectors stay within the realizable set. For the same reason, further reducing these models by, e.g., reduced-basis methods is not a simple task. Our new method overcomes these disadvantages of classical approaches. The coordinate transformation is performed on the semi-discretized level which makes them applicable to a wide range of kinetic schemes and replaces the nonlinear optimization problems by inversion of the positive-definite Hessian matrix. As a result, the new scheme gets rid of the realizability-related problems. Moreover, our numerical experiments demonstrate that our new method is often several times faster than the standard optimization-based scheme.

Keywords: moment models, minimum entropy, kinetic transport equation, model order reduction, realizability

1. Introduction

Kinetic equations play an important role in many physical applications. One of the earliest and most prominent examples is the Boltzmann equation which was derived by the Austrian physicist Ludwig Boltzmann in 1872 [6] and still forms the basis for the kinetic theory of rarefied gases. The Boltzmann equation or similar kinetic equations proved to be applicable not only to classical gases but also to electron transport in solids and plasmas, neutron transport in nuclear reactors, photon transport in superfluids and radiative transfer, among others [9, 26, 28–30]. More recently, kinetic equations were also derived in the context of biological modelling, e.g., for studying cell movement or wolf migration [7, 18, 21].

While analytic solutions can be derived in some special cases [16], usually kinetic equations have to be solved numerically. Due to their high dimensionality, directly solving kinetic equations with standard discretizations (e.g., finite difference methods) is often infeasible or restricted to very small grid sizes. For that reason,

¹**Funding:** The authors acknowledge funding by the Deutsche Forschungsgemeinschaft (DFG, German Research Foundation) under Germany’s Excellence Strategy EXC 2044 390685587, Mathematics Mnster: DynamicsGeometryStructure.

a variety of specialized approximate methods have been developed, many of which belong to the class of moment methods. Instead of computing the whole kinetic density function, moment approximations choose a set of weight functions (usually polynomials up to some order) on the velocity space and only track the weighted velocity averages (called moments) of the kinetic density with respect to these functions. This is usually done by performing a Galerkin projection of the original kinetic equation to the linear span of the weight functions. In general, the resulting moment equations are not closed and thus an ansatz for the velocity distribution has to be made. Choosing a linear combination of the weight functions gives the widely used P_N closure [28], where N is the degree of the highest-order moments in the model. The P_N closure results in linear equations, is simple to implement and often gives reasonable results. However, it does not guarantee non-negativity of the approximated kinetic density. This sometimes leads to physically meaningless solutions, as the P_N solutions can, e.g., contain negative values for the local particle density.

The so-called M_N [12, 32] models avoid these problems by choosing the ansatz function such that it minimizes an entropy functional which usually models the (negative) physical entropy. The resulting closed system of equations is hyperbolic and dissipates the chosen entropy [27]. However, numerically solving the M_N equations requires the solution of a non-linear optimization problem at every point on the space-time grid. Although the optimization problems can be solved in parallel [4, 20, 25, 36], the computational cost for high moment orders still is prohibitively high in practical applications. Another drawback of the entropy-based moment closures is that the optimization problem is solvable only for so-called realizable moment vectors, i.e., vectors that actually are moments of a positive density function. As explicit descriptions of the set of realizable moment vectors are usually not available, discretizations (especially of higher order) often struggle to keep the approximate solutions realizable [1, 10, 33, 37, 40, 43, 48].

A partial remedy for to the high computational cost of the minimum entropy models could be additional model reduction, for example via reduced basis methods [34]. These methods generate a reduced description of the (discretized) equations first and then use this reduced model to perform the actual computations. In some cases, e.g., if a given kinetic equation has to be solved many times for different parameters, this reduces overall computation time by several orders of magnitude. Generating the reduced model is usually done by constructing a low-dimensional linear subspace from solution trajectories and then projecting the problem to this subspace. This has been successfully done for the P_N models [22]. In the context of minimum-entropy moment models, however, this procedure is problematic as it does not preserve realizability, which may render the reduced model useless as it does not admit a solution.

Checking realizability is much easier when using piecewise linear bases instead of the standard polynomial basis on the whole velocity space [13, 14, 35, 42, 44–46]. In addition, the computational cost is significantly lower for these models. However, solving the optimization problems is still costly compared to linear models and maintaining realizability still requires additional limiters [44].

Another approach to fix the realizability issues is to introduce a regularization of the optimization problem [2]. The regularized problem admits a solution also for moments vectors that are not realizable and maintains most of the desirable properties of the original problem, at the cost of an additional approximation error (which, however, can be controlled by the regularization parameter). However, this approach still requires the solution of the (regularized) minimum entropy problem in each cell of the space-time grid.

In this paper, we will present a new discretization scheme for the minimum-entropy moment equations based on a coordinate-transformation of the semi-discretized equations. The new scheme replaces the non-linear optimization problems by matrix inversions and inherently guarantees realizability. As a consequence, the new scheme is often significantly faster than the untransformed scheme and shows improved parallel scaling. On the downside, adaptive timestepping is strictly needed for the transformed scheme. Moreover, numerically singular Hessian matrices will result in a failure of the scheme if no additional regularization is employed. However, we did not encounter such a situation during our extensive numerical experiments (despite the fact that the untransformed reference scheme had to use regularization in several of the tests).

This paper is organized as follows. First, in Section 2 we shortly recall the necessary background on minimum

entropy moment models. In Section 3, the new scheme is presented and analysed, followed by extensive numerical investigations in Section 4.

2. Minimum-entropy moment models

2.1. Kinetic transport equation

We consider the linear transport equation

$$\partial_t \psi + \boldsymbol{\Omega} \cdot \nabla_{\mathbf{x}} \psi + \sigma_a \psi = \sigma_s \mathcal{C}(\psi) + Q, \quad (2.1a)$$

which describes the density of particles with speed $\boldsymbol{\Omega} \in \mathcal{S}^2$ at position $\mathbf{x} \in X \subseteq \mathbb{R}^3$ and time $t \in T = [0, t_f]$ under the events of scattering (proportional to $\sigma_s(t, \mathbf{x})$), absorption (proportional to $\sigma_a(t, \mathbf{x})$) and emission (proportional to $Q(t, \mathbf{x}, \boldsymbol{\Omega})$). For simplicity, we will consider isotropic scattering

$$\mathcal{C}(\psi)(t, \mathbf{x}, \boldsymbol{\Omega}) = \frac{1}{|\mathcal{S}^2|} \int_{\mathcal{S}^2} \psi(t, \mathbf{x}, \boldsymbol{\Omega}') d\boldsymbol{\Omega}' - \psi(t, \mathbf{x}, \boldsymbol{\Omega}), \quad (2.1b)$$

isotropic time-independent source $Q(t, \mathbf{x}, \boldsymbol{\Omega}) = Q(\mathbf{x})$ and time-independent scattering $\sigma_s(t, \mathbf{x}) = \sigma_s(\mathbf{x})$ and absorption $\sigma_a(t, \mathbf{x}) = \sigma_a(\mathbf{x})$. The equation is supplemented with initial condition and Dirichlet boundary conditions:

$$\psi(0, \mathbf{x}, \boldsymbol{\Omega}) = \psi_{t=0}(\mathbf{x}, \boldsymbol{\Omega}) \quad \text{for } \mathbf{x} \in X, \boldsymbol{\Omega} \in \mathcal{S}^2 \quad (2.1c)$$

$$\psi(t, \mathbf{x}, \boldsymbol{\Omega}) = \psi_b(t, \mathbf{x}, \boldsymbol{\Omega}) \quad \text{for } t \in T, \mathbf{x} \in \partial X, \mathbf{n} \cdot \boldsymbol{\Omega} < 0 \quad (2.1d)$$

where \mathbf{n} is the outward unit normal vector in $\mathbf{x} \in \partial X$.

Parameterizing $\boldsymbol{\Omega}$ in spherical coordinates we obtain

$$\boldsymbol{\Omega} = \left(\sqrt{1 - \mu^2} \cos(\varphi), \sqrt{1 - \mu^2} \sin(\varphi), \mu \right)^T =: (\Omega_x, \Omega_y, \Omega_z)^T, \quad (2.2)$$

where $\varphi \in [0, 2\pi]$ is the azimuthal and $\mu \in [-1, 1]$ the cosine of the polar angle.

As a one-dimensional simplification, we will also consider the models in slab geometry, which is a projection of the sphere onto the z -axis [47]. The transport equation under consideration then has the form

$$\partial_t \psi + \mu \partial_z \psi + \sigma_a \psi = \sigma_s \mathcal{C}(\psi) + Q, \quad t \in T, z \in X, \mu \in [-1, 1]. \quad (2.3)$$

2.2. The moment approximation

In the following, V will always denote the angular domain, i.e., $V = [-1, 1]$ in slab geometry and $V = \mathcal{S}^2$ in the three-dimensional case, and $\boldsymbol{\Omega}$ will denote the corresponding angular variable. Moreover, we will use angle brackets to denote integration over V , i.e.,

$$\langle f \rangle := \int_V f(\boldsymbol{\Omega}) d\boldsymbol{\Omega}$$

for all $f \in L^1(V)$.

Due to the high-dimensionality, directly discretizing and solving (2.1) via standard numerical schemes is usually not viable. However, in many applications, we do not need the whole kinetic density but are only interested in the *local particle density*

$$\rho(t, \mathbf{x}) := \langle \psi(t, \mathbf{x}, \boldsymbol{\Omega}) \rangle. \quad (2.4)$$

We will thus consider moment approximations of (2.1). To that end, let $\mathbf{b} : V \rightarrow \mathbb{R}^n$ be a vector of n functions b_i , called the *moment basis functions*. The *moments* $\mathbf{u} = (u_0, \dots, u_{n-1})^T$ of a given distribution function ψ are then defined by

$$\mathbf{u}(t, \mathbf{x}) := \langle \mathbf{b}(\boldsymbol{\Omega})\psi(t, \mathbf{x}, \boldsymbol{\Omega}) \rangle \quad (2.5)$$

where the integration is performed component-wise. Equations for \mathbf{u} can be obtained by multiplying (2.1) with \mathbf{b} and integrating over V , resulting in the moment equations

$$\partial_t \mathbf{u} + \langle \mathbf{b} \nabla_{\mathbf{x}} \cdot (\boldsymbol{\Omega} \psi) \rangle + \sigma_a \mathbf{u} = \sigma_s \langle \mathbf{b} \mathcal{C}(\psi) \rangle + \langle \mathbf{b} Q \rangle. \quad (2.6)$$

Let $\boldsymbol{\alpha}_{\text{one}} \in \mathbb{R}^n$ be a vector such that $\boldsymbol{\alpha}_{\text{one}}^T \mathbf{b} \equiv 1$ (such a vector exists for all regarded basis [44]). Using (2.4) and (2.5), from \mathbf{u} we can get the local particle density as

$$\rho(\mathbf{u}) = \boldsymbol{\alpha}_{\text{one}}^T \mathbf{u}. \quad (2.7)$$

Depending on the choice of \mathbf{b} the terms $\langle \mathbf{b} \nabla_{\mathbf{x}} \cdot (\boldsymbol{\Omega} \psi) \rangle$ and $\langle \mathbf{b} \mathcal{C}(\psi) \rangle$ in (2.6) cannot be given explicitly in terms of the moments. Therefore an ansatz $\hat{\psi}_{\mathbf{u}}$ has to be made replacing ψ in the unclosed terms. Replacing ψ in (2.6) with $\hat{\psi}_{\mathbf{u}}$ yields a closed system of non-linear equations for \mathbf{u} :

$$\partial_t \mathbf{u} + \sum_{k=1}^d \partial_{x_k} \mathbf{f}_k(\mathbf{u}) = \mathbf{s}(\mathbf{x}, \mathbf{u}), \quad (2.8)$$

where

$$\mathbf{f}_k(\mathbf{u}) = \langle \Omega_k \mathbf{b} \hat{\psi}_{\mathbf{u}} \rangle \quad (2.9)$$

and

$$\mathbf{s}(\mathbf{x}, \mathbf{u}) = \sigma_s(\mathbf{x}) \langle \mathbf{b} \mathcal{C}(\hat{\psi}_{\mathbf{u}}) \rangle + \langle \mathbf{b} Q \rangle - \sigma_a \mathbf{u} \quad (2.10a)$$

$$= \frac{\sigma_s}{|V|} \langle \mathbf{b} \rangle \langle \hat{\psi}_{\mathbf{u}} \rangle + Q \langle \mathbf{b} \rangle - \sigma_t \mathbf{u} \quad (2.10b)$$

$$= \frac{\sigma_s}{|V|} \langle \mathbf{b} \rangle \boldsymbol{\alpha}_{\text{one}}^T \mathbf{u} + Q \langle \mathbf{b} \rangle - \sigma_t \mathbf{u} \quad (2.10c)$$

$$= \mathbf{G}(\mathbf{x}) \mathbf{u} + Q(\mathbf{x}) \langle \mathbf{b} \rangle. \quad (2.10d)$$

Here, $\sigma_t = \sigma_s + \sigma_a$, $G_{ij} = \frac{\sigma_s}{|V|} \langle b_i \rangle \alpha_{\text{one},j} - \sigma_t \delta_{ij}$, and we have used in (2.10b) the fact that we assumed isotropic scattering and isotropic source term (compare (2.1b)).

It remains to specify the basis functions and the ansatz density $\hat{\psi}_{\mathbf{u}}$.

2.3. Minimum entropy closure and choice of basis functions

For the minimum entropy closure [15, 27, 31, 32], we choose a strictly convex and twice continuously differentiable *entropy density function* $\eta : D \subset \mathbb{R} \rightarrow \mathbb{R}$ and demand that the ansatz function minimizes the entropy functional

$$\mathcal{H}(\psi) = \langle \eta(\psi) \rangle \quad (2.11)$$

under the moment constraints, i.e.,

$$\hat{\psi}_{\mathbf{u}} := \operatorname{argmin}_{\{\psi \in L^1(V) \mid \operatorname{Range}(\psi) \subset D\}} \{ \mathcal{H}(\psi) \mid \langle \mathbf{b} \psi \rangle = \mathbf{u} \}. \quad (2.12)$$

As in [20, 27, 45], for sake of simplicity, we focus on *Maxwell-Boltzmann entropy*

$$\eta(\psi) = \psi \log(\psi) - \psi, \quad (2.13)$$

which is used for non-interacting, classical particles as in an ideal gas. Thus, $D = (0, \infty)$ and (2.12) becomes

$$\hat{\psi}_{\mathbf{u}} := \operatorname{argmin}_{\psi \in L_+^1(V)} \{ \mathcal{H}(\psi) \mid \langle \mathbf{b}\psi \rangle = \mathbf{u} \}. \quad (2.14)$$

The minimization problem is typically solved through its strictly convex finite-dimensional dual,

$$\boldsymbol{\alpha}(\mathbf{u}) := \operatorname{argmin}_{\tilde{\boldsymbol{\alpha}} \in \mathbb{R}^n} \left\langle \eta_*(\mathbf{b}^T \tilde{\boldsymbol{\alpha}}) \right\rangle - \mathbf{u}^T \tilde{\boldsymbol{\alpha}}, \quad (2.15)$$

where η_* is the Legendre dual of η . The first-order necessary conditions for the multipliers $\boldsymbol{\alpha}(\mathbf{u})$ show that the solution to (2.12), if it exists, has the form

$$\hat{\psi}_{\mathbf{u}} = \eta'_* \left(\mathbf{b}^T \boldsymbol{\alpha}(\mathbf{u}) \right), \quad (2.16)$$

where η'_* is the derivative of η_* . With Maxwell-Boltzmann entropy, $\eta_*(p) = \eta'_*(p) = \exp(p)$ and the minimum entropy ansatz (2.16) becomes $\hat{\psi}_{\mathbf{u}} = \exp \left(\mathbf{b}^T \boldsymbol{\alpha}(\mathbf{u}) \right)$.

We will consider three options for the basis functions \mathbf{b} . The full moment basis \mathbf{f}_N is the standard choice and consists of polynomials of up to order N , resulting in $n = N + 1$ and $n = (N + 1)^2$ basis functions in one and three dimensions, respectively. We will use Legendre polynomials in slab geometry and real spherical harmonics in the full three-dimensional setting.

For the other two bases, we choose a triangulation \mathcal{P} of the velocity domain V into intervals (slab geometry) or spherical triangles (three dimensions). In this paper, in three dimensions, the triangulation will always be obtained by dyadic refinement of the octants of the sphere. In slab geometry, we will always use equidistant intervals. Let n_v and n_t be the number of nodes and elements of the triangulation, respectively. Similar to the linear basis typically used in the continuous finite element method, the hat function basis \mathbf{h}_n with $n = n_v$ basis functions then consists of the continuous piecewise linear functions that evaluate to 1 at one node of the triangulation and to 0 at all other nodes. The partial moment basis \mathbf{p}_n is defined in analogy to the discontinuous finite element method and consists of the $n = 2n_t$ or $n = 4n_t$ (in one and three dimensions, respectively) basis functions for the space of piecewise linear functions on \mathcal{P} that may be discontinuous between elements of the triangulation. See [45] for a more detailed definitions of these bases.

Models using the full moment basis show optimal (spectral) convergence for smooth problems. For non-smooth problems, however, \mathbf{p}_n and \mathbf{h}_n bases might be more suitable as they show similar approximation quality and avoid many of the performance and realizability problems of the classical polynomial models [44, 45].

2.4. Realizability

The minimization problem (2.14) is solvable if the moment vector lies in the *positively realizable set* [24, 45]

$$\mathcal{R}_{\mathbf{b}}^+ := \{ \mathbf{u} \in \mathbb{R}^n \mid \exists \psi \in L_+^1(V) \text{ such that } \mathbf{u} = \langle \mathbf{b}\psi \rangle \}. \quad (2.17)$$

where

$$L_+^1 := \{ \psi \in L^1(V) \mid \psi > 0 \text{ almost everywhere. } \} \quad (2.18)$$

is the space of positive integrable functions. In fact, the map $\boldsymbol{\alpha} : \mathcal{R}_{\mathbf{b}}^+ \rightarrow \mathbb{R}^n$ given by (2.15) is a diffeomorphism with inverse map

$$\mathbf{u} : \mathbb{R}^n \rightarrow \mathcal{R}_{\mathbf{b}}^+, \quad \mathbf{u}(\boldsymbol{\alpha}) := \langle \mathbf{b} \exp(\boldsymbol{\alpha}^T \mathbf{b}) \rangle. \quad (2.19)$$

The realizable set is a convex cone that, depending on the choice of basis \mathbf{b} , may have a complicated structure. For the full moment basis, a moment vector \mathbf{u} is realizable if some (\mathbf{u} -dependent) Hankel matrices are positive definite [11]. This criterion is hard to test in practice, especially for large polynomial order N . In contrast, the realizability conditions for the piecewise linear bases are quite simple [45]. In particular, a moment vector is realizable with respect to \mathbf{h}_n if all its entries are positive [41, 45]:

$$\mathcal{R}_{\mathbf{h}_n}^+ := \{ \mathbf{u} \in \mathbb{R}^n \mid u_i > 0 \text{ for all } i \in \{1, \dots, n\} \}. \quad (2.20)$$

In general, we cannot calculate the integral in the definition of the realizable set (2.17) exactly. We thus choose a quadrature

$$\mathcal{Q} = \{ (w_i, \boldsymbol{\Omega}_i) \in \mathbb{R}^+ \times V \mid i \in \{1, \dots, n_{\mathcal{Q}}\} \} \quad (2.21)$$

with positive weights w_i and define the \mathcal{Q} -realizable set

$$\mathcal{R}_{\mathbf{b}}^{\mathcal{Q}} := \{ \mathbf{u} \in \mathbb{R}^n \mid \exists \psi(\boldsymbol{\Omega}) \geq 0 \text{ such that } \mathbf{u} = \langle \mathbf{b}\psi \rangle_{\mathcal{Q}} := \sum_{i=1}^{n_{\mathcal{Q}}} w_i \mathbf{b}(\boldsymbol{\Omega}_i) \psi(\boldsymbol{\Omega}_i) \} \quad (2.22)$$

Note that we used non-negative functions in (2.22) instead of positive functions as in (2.17) to simplify notation later on.

The \mathcal{Q} -realizable set is a subset of the closure of the positively realizable set, i.e., $\mathcal{R}_{\mathbf{b}}^{\mathcal{Q}} \subset \overline{\mathcal{R}_{\mathbf{b}}^+}$ [3, 45]. For the full moment basis, $\mathcal{R}_{\mathbf{b}}^+ \setminus \mathcal{R}_{\mathbf{b}}^{\mathcal{Q}}$ is non-empty such that there are realizable moments that can not be realized numerically [3]. For the hat function bases, however, the two sets agree, i.e., $\mathcal{R}_{\mathbf{b}}^{\mathcal{Q}} = \overline{\mathcal{R}_{\mathbf{b}}^+}$, if the quadrature contains the nodes of the triangulation. For the partial moment basis, this is only true in slab geometry [45].

If we restrict the local particle density ρ (see (2.7)), the \mathcal{Q} -realizable set can be described as the convex hull of the basis function values at the quadrature nodes [3, 44]

$$\mathcal{R}_{\mathbf{b}}^{\mathcal{Q}}|_{\rho \leq 1} = \text{conv}(\mathbf{0}, \{\mathbf{b}(\boldsymbol{\Omega}_i)\}_{i=1}^{n_{\mathcal{Q}}}). \quad (2.23)$$

Thus, $\mathcal{R}_{\mathbf{b}}^{\mathcal{Q}}|_{\rho \leq 1}$ is a convex polytope and admits a description as the intersection of half-spaces

$$\mathcal{R}_{\mathbf{b}}^{\mathcal{Q}}|_{\rho \leq 1} = \{ \mathbf{u} \in \mathbb{R}^n \mid \tilde{\mathbf{C}}\mathbf{u} \leq \tilde{\mathbf{c}} \}, \quad (2.24)$$

where the inequality has to be read component-wise. As $\rho = \boldsymbol{\alpha}_{\text{one}}^T \mathbf{u}$ for all regarded bases, the condition $\rho \leq 1$ is one of these half-space inequalities. Removing this inequality, a half-space description of the unconstrained numerically realizable set is obtained.

$$\mathcal{R}_{\mathbf{b}}^{\mathcal{Q}} = \{ \mathbf{u} \in \mathbb{R}^n \mid \mathbf{C}\mathbf{u} \leq \mathbf{c} \}, \quad (2.25)$$

However, note that due to the high dimension and large number of facets computing (the half-space representation of) the convex hull is usually not feasible in practice[41].

3. Discretization

We consider two discretization schemes for the moment equations (2.8), a standard finite volume scheme (Section 3.1) and a new scheme based on the identification (2.19) between realizable set and \mathbb{R}^N (Section 3.2). For simplicity, we will restrict ourselves to first-order schemes. For both schemes, to compute the integrals we use Gauss-Lobatto quadratures and Fekete quadratures in one and three dimensions, respectively, using the same quadrature orders as in [44]. Thus, as investigated in [44], the quadrature error should be negligible.

3.1. Standard finite volume scheme

The reference scheme is a standard first-order finite volume scheme. Let $\{T_i\}_i$ be a numerical grid for the spatial domain X such that

$$X = \bigcup_i T_i \quad (3.1)$$

and define

$$\mathbf{u}_i(t) = \frac{1}{|T_i|} \int_{T_i} \mathbf{u}(t, \mathbf{x}) d\mathbf{x} \quad (3.2)$$

Integrating (2.8) over a grid cell T_i and dividing by $|T_i|$ gives (assuming the parameters σ_s, σ_t, Q are constant on that grid cell or doing a second-order approximation by using the midpoint rule for the source term)

$$\partial_t \mathbf{u}_i + \frac{1}{|T_i|} \int_{T_i} \sum_{k=1}^d \partial_{x_k} \mathbf{f}_k(\mathbf{u}) = \mathbf{s}(\mathbf{u}_i), \quad (3.3)$$

By applying the divergence theorem, we arrive at

$$\partial_t \mathbf{u}_i + \frac{1}{|T_i|} \sum_j \int_{S_{ij}} \mathbf{F}(\mathbf{u}) \cdot \mathbf{n}_{ij} = \mathbf{s}(\mathbf{u}_i) \quad (3.4)$$

where $S_{ij} = T_i \cap T_j$, the j -sum goes over all neighbors T_j of T_i and the flux matrix $\mathbf{F}(\mathbf{u}) \in \mathbb{R}^{n \times d}$ has entries $F_{lk} = (\mathbf{f}_k)_l$.

Replacing the flux term by a numerical flux \mathbf{g}_{ij} on S_{ij} , we get the semidiscrete form

$$\partial_t \mathbf{u}_i + \frac{1}{|T_i|} \sum_j \mathbf{g}_{ij}(\mathbf{u}_i, \mathbf{u}_j) = \mathbf{s}(\mathbf{u}_i) \quad (3.5)$$

In principle, we could use any numerical flux for hyperbolic equations, e.g. the Lax-Friedrichs flux. We will, however, use a numerical flux which is especially designed for the equations under consideration. Define the two half integrals

$$\langle b \rangle_{+, \mathbf{n}} = \int_{V^{+, \mathbf{n}}} b d\Omega \quad \text{and} \quad \langle b \rangle_{-, \mathbf{n}} = \int_{V^{-, \mathbf{n}}} b d\Omega \quad (3.6)$$

$$(3.7)$$

where

$$V^{+, \mathbf{n}} = \{ \Omega \in V \mid \Omega \cdot \mathbf{n} > 0 \}, \quad (3.8)$$

$$V^{-, \mathbf{n}} = \{ \Omega \in V \mid \Omega \cdot \mathbf{n} < 0 \}. \quad (3.9)$$

In the following, we will omit the normal vector if it is clear from the context and write, e.g., $\langle \cdot \rangle_+$ instead of $\langle \cdot \rangle_{+, \mathbf{n}}$ in these cases. The kinetic flux is defined as [14, 20]

$$\mathbf{g}_{ij}^{kin}(\mathbf{u}_i, \mathbf{u}_j) = \left(\left\langle (\Omega \cdot \mathbf{n}_{ij}) \hat{\psi}_{\mathbf{u}_i} \mathbf{b} \right\rangle_{+, \mathbf{n}_{ij}} + \left\langle (\Omega \cdot \mathbf{n}_{ij}) \hat{\psi}_{\mathbf{u}_j} \mathbf{b} \right\rangle_{-, \mathbf{n}_{ij}} \right) |S_{ij}| \quad (3.10)$$

Using the kinetic flux, the semidiscrete form (3.5) becomes

$$\partial_t \mathbf{u}_i + \sum_j \frac{|S_{ij}|}{|T_i|} \left(\left\langle (\Omega \cdot \mathbf{n}_{ij}) \hat{\psi}_{\mathbf{u}_i} \mathbf{b} \right\rangle_+ + \left\langle (\Omega \cdot \mathbf{n}_{ij}) \hat{\psi}_{\mathbf{u}_j} \mathbf{b} \right\rangle_- \right) = \mathbf{s}(\mathbf{u}_i) \quad (3.11)$$

We will then use an explicit one-step scheme for the time discretization. For example, an explicit Euler discretization gives the fully discrete form

$$\mathbf{u}_i^{\kappa+1} = \mathbf{u}_i^\kappa - \Delta t \left(\sum_j \frac{|S_{ij}|}{|T_i|} \left(\langle (\boldsymbol{\Omega} \cdot \mathbf{n}_{ij}) \hat{\psi}_{\mathbf{u}_i^\kappa} \mathbf{b} \rangle_+ + \langle (\boldsymbol{\Omega} \cdot \mathbf{n}_{ij}) \hat{\psi}_{\mathbf{u}_j^\kappa} \mathbf{b} \rangle_- \right) - \mathbf{s}(\mathbf{u}_i^\kappa) \right) \quad (3.12)$$

where \mathbf{u}_i^κ is the approximation of \mathbf{u}_i at time step κ .

The scheme (3.12) requires the solution of the minimization problem (2.14) in every time step on each grid cell. The initial values thus have to be realizable and we have to limit the time step Δt to ensure that the scheme yields realizable moments.

Theorem 3.1. *The numerical scheme (3.12) using a structured cubic grid with equally-sized grid cells with edge length Δx is realizability-preserving under the CFL-like condition*

$$\Delta t < \frac{1}{\sigma_t + \frac{\sqrt{d}}{\Delta x}}. \quad (3.13)$$

Proof. We will generalise the proof of [41, Corollary 3.17] to several dimensions. Let \mathbf{u}_i^κ be realizable. By (3.11) and (2.10b), we have

$$\begin{aligned} \mathbf{u}_i^{\kappa+1} &= \left\langle \mathbf{b} \left(\hat{\psi}_{\mathbf{u}_i^\kappa} - \Delta t \left(\sum_j \frac{|S_{ij}|}{|T_i|} \left((\boldsymbol{\Omega} \cdot \mathbf{n}_{ij})^+ \hat{\psi}_{\mathbf{u}_i^\kappa} + (\boldsymbol{\Omega} \cdot \mathbf{n}_{ij})^- \hat{\psi}_{\mathbf{u}_j^\kappa} \right) - \frac{\sigma_s}{|V|} \langle \hat{\psi}_{\mathbf{u}_i^\kappa} \rangle - Q + \sigma_t \hat{\psi}_{\mathbf{u}_i^\kappa} \right) \right) \right\rangle \\ &=: \langle \mathbf{b} \psi_i^{\kappa+1} \rangle. \end{aligned}$$

where $(\boldsymbol{\Omega} \cdot \mathbf{n}_{ij})^+ = \max(\boldsymbol{\Omega} \cdot \mathbf{n}_{ij}, 0)$ and $(\boldsymbol{\Omega} \cdot \mathbf{n}_{ij})^- = \min(\boldsymbol{\Omega} \cdot \mathbf{n}_{ij}, 0)$. We have to show that $\psi_i^{\kappa+1}$ is positive for all $\boldsymbol{\Omega} \in \mathcal{S}^2$ under the time step restriction (3.13). Neglecting positive terms, we arrive at

$$\psi_i^{\kappa+1} \geq \left(1 - \Delta t \left(\sigma_t + \sum_j \frac{|S_{ij}|}{|T_i|} (\boldsymbol{\Omega} \cdot \mathbf{n}_{ij})^+ \right) \right) \hat{\psi}_{\mathbf{u}_i^\kappa} \quad (3.14)$$

For a structured cubic grid with equally-sized grid cells, we have $\frac{|S_{ij}|}{|T_i|} = \frac{1}{\Delta x}$ for all (i, j) and $\sum_j (\boldsymbol{\Omega} \cdot \mathbf{n}_{ij})^+ = \|\boldsymbol{\Omega}\|_1 \leq \sqrt{d}$ and thus (3.14) becomes

$$\psi_i^{\kappa+1} \geq \left(1 - \Delta t \left(\sigma_t + \frac{\sqrt{d}}{\Delta x} \right) \right) \hat{\psi}_{\mathbf{u}_i^\kappa}$$

which is positive if (3.13) holds. \square

Note that we assumed in the proof that the optimization problems are solved exactly (by using $\hat{\psi}_{\mathbf{u}_i^\kappa}$). To account for inexact solutions, we will always multiply the time step restriction by a safety factor of 0.9 in our numerical experiments (see [44] for more details).

The time step restriction due to the crosssection σ_t can be avoided, e.g, by using implicit-explicit methods where the source term is treated implicitly [38–40, 44]. As in [44], we will use a second-order Strang splitting scheme for the splitted system

$$\partial_t \mathbf{u}_i = - \frac{1}{|T_i|} \sum_j \mathbf{g}_{ij}(\mathbf{u}_i, \mathbf{u}_j) \quad (3.15a)$$

$$\partial_t \mathbf{u}_i = \mathbf{s}(\mathbf{x}, \mathbf{u}_i), \quad (3.15b)$$

i.e., in each time step from t to $t + \Delta t$ we first solve the (linear) source system (3.15b) analytically (using matrix exponentials), up to the time $t + \frac{\Delta t}{2}$, then we use the result as input to solve the hyperbolic part (3.15a) with a full timestep Δt , then we again advance (3.15b) analytically for a half time step $\frac{\Delta t}{2}$. As the source system is solved analytically (and thus preserves realizability), we only have to ensure that realizability is preserved when solving the hyperbolic part. We can thus avoid the time step restriction due to the crosssection σ_t .

Corollary 3.2. *The splitting scheme based on (3.15) is realizability-preserving under the CFL-like condition*

$$\Delta t < \frac{\Delta x}{\sqrt{d}}. \quad (3.16)$$

If we advance the hyperbolic system (3.15a) in time by strong-stability preserving Runge-Kutta schemes [17] the CFL condition (3.16) still holds as these schemes consist of convex combinations of forward Euler steps. In particular, we will use Heun's method in all tests which is of second order. The optimization problems are solved using a backtracking Newton scheme for (2.15). To handle ill-conditioned problems, we use (depending on the basis \mathbf{b}) adaptive change of basis [3] and isotropic regularization [4]

$$\mathbf{u}^r := (1 - r)\mathbf{u} + r\mathbf{u}_{\text{iso}}. \quad (3.17)$$

For more details on the implementation see [44].

3.2. New scheme in transformed variables

For the second scheme, we will use the identification between the realizable set $\mathcal{R}_{\mathbf{b}}^+$ and \mathbb{R}^n given by the diffeomorphism (2.19). Note that

$$\frac{d\mathbf{u}}{d\boldsymbol{\alpha}} = \frac{d}{d\boldsymbol{\alpha}} \left(\langle \mathbf{b} \hat{\psi}_{\mathbf{u}} \rangle \right) \stackrel{(2.16)}{=} \frac{d}{d\boldsymbol{\alpha}} \left(\langle \mathbf{b} \eta'_*(\boldsymbol{\alpha}^T \mathbf{b}) \rangle \right) = \langle \mathbf{b} \mathbf{b}^T \eta''_*(\boldsymbol{\alpha}^T \mathbf{b}) \rangle =: \mathbf{H}(\boldsymbol{\alpha}) \quad (3.18)$$

is positive definite (as η and thus also η_* is strictly convex) and for

$$\mathbf{f}_k(\boldsymbol{\alpha}) = \langle \Omega_k \mathbf{b} \eta'_*(\boldsymbol{\alpha}^T \mathbf{b}) \rangle \quad (3.19)$$

(compare (2.9)) we have

$$\frac{d\mathbf{f}_k}{d\boldsymbol{\alpha}} = \langle \Omega_k \mathbf{b} \mathbf{b}^T \eta''_*(\boldsymbol{\alpha}^T \mathbf{b}) \rangle =: \mathbf{J}(\boldsymbol{\alpha}). \quad (3.20)$$

In transformed coordinates, assuming \mathbf{u} is sufficiently smooth, (2.8) thus becomes [27]

$$\begin{aligned} \mathbf{s}(\mathbf{u}(\boldsymbol{\alpha})) &= \partial_t \mathbf{u}(\boldsymbol{\alpha}) + \sum_{k=1}^d \partial_{x_k} \mathbf{f}_k(\mathbf{u}(\boldsymbol{\alpha})) \\ &= \frac{d\mathbf{u}}{d\boldsymbol{\alpha}}(\boldsymbol{\alpha}) \partial_t \boldsymbol{\alpha} + \sum_{k=1}^d \frac{d\mathbf{f}_k}{d\boldsymbol{\alpha}}(\boldsymbol{\alpha}) \partial_{x_k} \boldsymbol{\alpha} \\ &= \mathbf{H}(\boldsymbol{\alpha}) \partial_t \boldsymbol{\alpha} + \sum_{k=1}^d \mathbf{J}(\boldsymbol{\alpha}) \partial_{x_k} \boldsymbol{\alpha} \end{aligned} \quad (3.21)$$

A numerical scheme based on the form (3.21) could potentially be much faster than the scheme (3.12) as it avoids solving the nonlinear optimization problem and only needs inversion of the positive definite symmetric

matrix $\mathbf{H}(\boldsymbol{\alpha})$. However, (3.21) is not in conservation form which makes it hard to guarantee that numerical schemes converge to the correct weak solution of (2.8).

On the other hand, if we perform the space discretization first and then transform the semi-discrete equation (3.5) to the new coordinates, we arrive at

$$\mathbf{H}(\boldsymbol{\alpha}_i) \partial_t \boldsymbol{\alpha}_i + \frac{1}{|T_i|} \sum_j \mathbf{g}_{ij}(\mathbf{u}(\boldsymbol{\alpha}_i), \mathbf{u}(\boldsymbol{\alpha}_j)) = \mathbf{s}(\mathbf{u}(\boldsymbol{\alpha}_i)) \quad (3.22)$$

and we can show that this scheme converges to the same solution as the direct finite volume discretization (3.5) if the same time discretization is used. In the following theorem, we will use a fixed time step Δt . This is only for notational simplicity, the theorem can easily be generalized to varying time steps.

Theorem 3.3. *Let $t_\kappa := \kappa \cdot \Delta t$ and let $\bar{\mathbf{u}}$ be the piecewise constant function*

$$\bar{\mathbf{u}}(t, \mathbf{x}) := \mathbf{u}_i^\kappa \text{ if } t \in [t_\kappa, t_{\kappa+1}), \mathbf{x} \in T_i$$

where the values \mathbf{u}_i^κ are obtained from the explicit one-step time discretization

$$\mathbf{u}_i^{\kappa+1} = \mathbf{u}_i^\kappa + \Delta t \Phi(\mathbf{u}_0^\kappa, \mathbf{u}_1^\kappa, \dots, \mathbf{u}_I^\kappa)$$

of the semidiscrete finite volume scheme (3.5). Let further

$$\bar{\boldsymbol{\alpha}}(t, \mathbf{x}) := \boldsymbol{\alpha}_i^\kappa \text{ if } t \in [t_\kappa, t_{\kappa+1}), \mathbf{x} \in T_i$$

be the piecewise constant function obtained from the corresponding discretization

$$\boldsymbol{\alpha}_i^{\kappa+1} = \boldsymbol{\alpha}_i^\kappa + \Delta t \mathbf{H}(\boldsymbol{\alpha}_i^\kappa)^{-1} \Phi(\mathbf{u}(\boldsymbol{\alpha}_0^\kappa), \mathbf{u}(\boldsymbol{\alpha}_1^\kappa), \dots, \mathbf{u}(\boldsymbol{\alpha}_I^\kappa)) \quad (3.23)$$

of the transformed semidiscrete equation (3.22). Then

$$\mathbf{u}(\bar{\boldsymbol{\alpha}}(t, \mathbf{x})) = \bar{\mathbf{u}}(t, \mathbf{x}) + O(\Delta t)$$

Proof. We will show that the local truncation error is of second order by applying the diffeomorphism (2.19) to (3.23) and then using a first-order Taylor expansion. Let $\mathbf{u}(\boldsymbol{\alpha}_j^\kappa) = \mathbf{u}_j^\kappa$ for all $j = 1, \dots, I$. Then we have

$$\begin{aligned} \mathbf{u}(\boldsymbol{\alpha}_i^{\kappa+1}) &= \mathbf{u}\left(\boldsymbol{\alpha}_i^\kappa + \Delta t \mathbf{H}(\boldsymbol{\alpha}_i^\kappa)^{-1} \Phi(\mathbf{u}(\boldsymbol{\alpha}_0^\kappa), \mathbf{u}(\boldsymbol{\alpha}_1^\kappa), \dots, \mathbf{u}(\boldsymbol{\alpha}_I^\kappa))\right) \\ &= \mathbf{u}(\boldsymbol{\alpha}_i^\kappa) + \frac{d\mathbf{u}}{d\boldsymbol{\alpha}}(\boldsymbol{\alpha}_i^\kappa) \Delta t \mathbf{H}(\boldsymbol{\alpha}_i^\kappa)^{-1} \Phi(\mathbf{u}(\boldsymbol{\alpha}_0^\kappa), \mathbf{u}(\boldsymbol{\alpha}_1^\kappa), \dots, \mathbf{u}(\boldsymbol{\alpha}_I^\kappa)) + O(\Delta t^2) \\ &\stackrel{(3.18)}{=} \mathbf{u}(\boldsymbol{\alpha}_i^\kappa) + \Delta t \Phi(\mathbf{u}(\boldsymbol{\alpha}_0^\kappa), \mathbf{u}(\boldsymbol{\alpha}_1^\kappa), \dots, \mathbf{u}(\boldsymbol{\alpha}_I^\kappa)) + O(\Delta t^2) \\ &= \mathbf{u}_i^{\kappa+1} + O(\Delta t^2) \end{aligned} \quad \square$$

In addition, the order of convergence of the time stepping scheme is preserved by the transformation.

Theorem 3.4. *Let $\{\mathbf{u}_i^\kappa\}, \{\boldsymbol{\alpha}_i^\kappa\}$ as in Theorem 3.3 and let $\mathbf{u}_i(t)$ and $\boldsymbol{\alpha}_i(t)$ be the solutions of (3.5) and (3.22), respectively. If the time stepping scheme is of order k , i.e., if*

$$\boldsymbol{\alpha}_i^\kappa = \boldsymbol{\alpha}_i(t_\kappa) + O(\Delta t^k),$$

then the corresponding moments converge with the same order, i.e.,

$$\mathbf{u}(\boldsymbol{\alpha}_i^\kappa) = \mathbf{u}_i(t_\kappa) + O(\Delta t^k).$$

Proof.

$$\mathbf{u}(\boldsymbol{\alpha}_i^\kappa) = \mathbf{u}(\boldsymbol{\alpha}_i(t_\kappa) + O(\Delta t^\kappa)) = \mathbf{u}(\boldsymbol{\alpha}_i(t_\kappa)) + \mathbf{H}(\boldsymbol{\alpha}_i(t_\kappa))O(\Delta t^\kappa) = \mathbf{u}_i(t_\kappa) + O(\Delta t^\kappa).$$

□

Using the explicit Euler scheme and the kinetic flux (3.10), the fully discrete form is

$$\boldsymbol{\alpha}_i^{\kappa+1} = \boldsymbol{\alpha}_i^\kappa + \Delta t \mathbf{H}(\boldsymbol{\alpha}_i)^{-1} \left(\mathbf{s}(\mathbf{u}(\boldsymbol{\alpha}_i)) - \sum_j \frac{|S_{ij}|}{|T_i|} \left(\langle (\boldsymbol{\Omega} \cdot \mathbf{n}_{ij}) \eta'_*(\boldsymbol{\alpha}_i^T \mathbf{b}) \rangle_+ + \langle (\boldsymbol{\Omega} \cdot \mathbf{n}_{ij}) \eta'_*(\boldsymbol{\alpha}_j^T \mathbf{b}) \rangle_- \right) \right). \quad (3.24)$$

As we do not have an estimate on a suitable time step size, instead of using a fixed time step we will use the adaptive Runge-Kutta method by Bogacki and Shampine [5]. As an error measure, we use the mixed error [19, Chapter II.4, Equation (4.11)]

$$\text{err} = \max_{l=1, \dots, I \cdot n} \frac{|\alpha_{1,l} - \alpha_{2,l}|}{\tau_{abs} + \max(\alpha_{1,l}, \alpha_{2,l}) \tau_{rel}} \quad (3.25)$$

and recompute with halved time step $\frac{dt}{2}$ if $\text{err} > 1$ or if an exception is thrown during the computation (e.g., if a matrix inversion fails or `infs` or `NaNs` are detected in the results). For simplicity, we will always use $\tau_{abs} = \tau_{rel} = \tau$ in the following.

Other than the standard discretization (3.12), the scheme (3.24) does not involve solving an optimization problem on each grid cell in each time step. Instead, the positive definite Hessian \mathbf{H} has to be inverted. In addition, we do not need a time step restriction to ensure realizability, as the multipliers $\boldsymbol{\alpha}$ can take values in the whole \mathbb{R}^n . Note that we still have to solve the optimization problem once in each grid cell to obtain the initial values $\{\boldsymbol{\alpha}_i^0\}$. However, often the initial values are simple (e.g., constant) such that this is not a major issue. In particular, we usually do not have to implement special techniques for ill-conditioned problems like adaptive quadrature [4] or adaptive change of basis [3].

4. Numerical Experiments

We investigate the behavior of the new scheme in several benchmarks. We use the same tests as in [44]. In the following, we will briefly restate the test cases. For a more detailed description and plots of (numerical) solutions see [44] and references therein. As the minimum entropy models cannot handle zero densities, we use the small isotropic distribution $\psi_{\text{vac}} = 0.5 \cdot 10^{-6}$ to approximate a vacuum. Note that we increased the vacuum density slightly compared to [44] to avoid numerical difficulties with very low densities. We use the following test cases:

- *Planesource.* In this test case, all mass is concentrated in the middle of the computational domain $X = [-1.2, 1.2]$, i.e., we use the isotropic initial distribution

$$\psi_{t=0}(z, \mu) = \psi_{\text{vac}} + \delta(z) \text{ for } z \in X.$$

The physical coefficients are set to $\sigma_s \equiv 1$, $\sigma_a \equiv 0$ and $Q \equiv 0$. Vacuum boundary conditions are used.

- *Sourcebeam.* In this test case, a strongly anisotropic beam enters the computational domain $X = [0, 3]$ from the left. In addition, a source is present in the interval $[1, 1.5]$. More precisely, the approximate vacuum is used as initial condition and boundary condition on the right-hand side, and the left boundary distribution is

$$\psi_b(t, 0, \mu) = \frac{e^{-10^5(\mu-1)^2}}{\langle e^{-10^5(\mu-1)^2} \rangle}$$

The parameters are set to

$$\sigma_a(z) = \begin{cases} 1 & \text{if } z \leq 2, \\ 0 & \text{else,} \end{cases} \quad \sigma_s(z) = \begin{cases} 0 & \text{if } z \leq 1, \\ 2 & \text{if } 1 < z \leq 2, \\ 10 & \text{else} \end{cases} \quad Q(z) = \begin{cases} \frac{1}{2} & \text{if } 1 \leq z \leq 1.5, \\ 0 & \text{else,} \end{cases}$$

- *Pointsource.* The point-source test is a smoothed three-dimensional analogue of the plane-source test. The initial condition in the domain $X = [-1, 1]^3$ is

$$\psi_{t=0}(\mathbf{x}, \boldsymbol{\Omega}) = \psi_{\text{vac}} + \frac{1}{4\pi^4 \sigma^3} \exp\left(-\frac{|\mathbf{x}|^2}{\pi \sigma^2}\right),$$

where $\sigma = 0.03$. The parameters are the same as in the plane-source test.

- *Checkerboard.* The checkerboard test case is loosely based on a part of a reactor core [8]. The domain $X = [0, 7]^3$ is split into scattering and absorbing regions, $X = X_s \cup X_a$, where

$$X_a = \left\{ \mathbf{x} = (x, y, z)^T \in [1, 6]^3 \mid \begin{array}{l} ([x] + [y] + [z]) \bmod 2 = 1, \\ \mathbf{x} \notin [3, 4]^3 \cup [3, 4] \times [5, 6] \times [3, 4] \end{array} \right\}$$

The parameters are

$$\sigma_s(\mathbf{x}) = \begin{cases} 1 & \text{if } \mathbf{x} \in X_s, \\ 0 & \text{else,} \end{cases}, \quad \sigma_a(\mathbf{x}) = \begin{cases} 0 & \text{if } \mathbf{x} \in X_s, \\ 10 & \text{else,} \end{cases}, \quad Q(\mathbf{x}) = \begin{cases} \frac{1}{4\pi} & \text{if } \mathbf{x} \in [3, 4]^3, \\ 0 & \text{else.} \end{cases}$$

Vacuum initial and boundary conditions are used.

- *Shadow.* The shadow test case represents an isotropic particle stream that is partially blocked by an absorber, resulting in a shadowed region behind the absorber. The particle stream is given by an isotropic boundary condition with density $\rho = 2$ at $x = 0$. On the other boundaries of the domain $X = [0, 12] \times [0, 4] \times [0, 3]$ and as an initial condition, the approximate vacuum is prescribed. The parameters are as follows:

$$\sigma_s(\mathbf{x}) = Q(\mathbf{x}) = 0$$

$$\sigma_a(\mathbf{x}) = \begin{cases} 50 & \text{if } \mathbf{x} \in [2, 3] \times [1, 3] \times [0, 2] \\ 0 & \text{else,} \end{cases}$$

Whenever we need a reference scheme, we use the splitting scheme based on 3.15. The obvious choice might be the unsplit scheme (3.12), as the new scheme is just a coordinate transformation of this scheme. However, the splitting scheme is easy to implement and avoids the time step restriction due to the physical parameters. For the new scheme, a similar splitting approach is not straightforward. Thus, using (3.12) as a reference would arguably give the new scheme an unfair advantage.

4.1. Convergence

First, we validate numerically that the new scheme (3.24) converges to the same solution as the splitting scheme (3.15). For that purpose, we solve the Planesource test case (slab geometry) and the Pointsource test case (three dimensions) with both schemes for varying tolerance and time step parameter, respectively, and calculate the errors with respect to a reference solution (new scheme with $\tau = 1e-9$). As error measure, we choose the L^1 -error of the piecewise constant finite volume approximations

$$E_h^1(\mathbf{u}) = \|\mathbf{u} - \mathbf{u}_{\text{ref}}\|_{L^1(X)}. \quad (4.1)$$

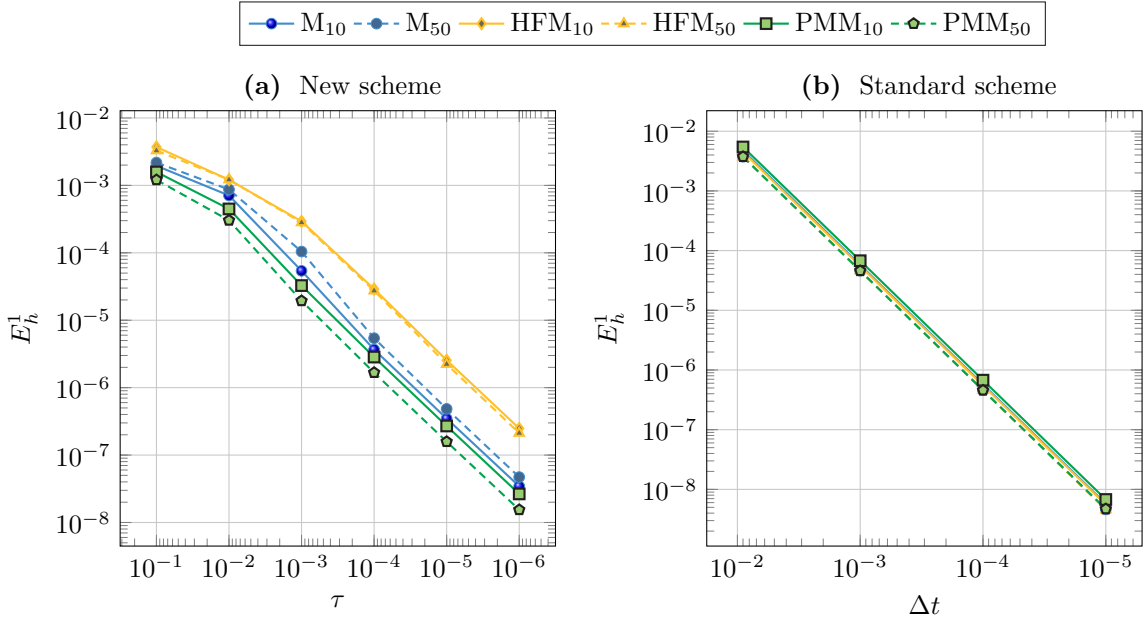


Figure 4.1: L^1 -error against reference solution (new scheme with $\tau = 10^{-9}$) in the planesource test case ($I = 240, t_f = 0.5$). (a) New scheme for decreasing tolerance parameter τ . (b) Standard scheme for decreasing time step Δt .

We use a relatively coarse grid for both testcases to be able to compute the results for very small tolerance parameter τ or time step Δt in reasonable time. However, for large parameters ($\tau = 10^{-2}, 10^{-3}$, $\Delta t = \Delta t_{max}$) we confirmed that the results are similar for the other testcases (Sourcebeam, Checkerboard, Shadow) and the grid sizes and final times used in the next subsection 4.2 (see Tables A.1 and A.2).

As can be seen in Figures 4.1 and 4.2, both schemes nicely converge to the reference solution. For the standard scheme, the error is basically independent of the model which is not true for the new scheme. This is probably due to the fact that for the new scheme, the error estimate during the time stepping is calculated in transformed (α -)coordinates while the final error is plotted in the original (\mathbf{u} -)coordinates. The L^∞ -errors behave similarly (data not shown).

For large tolerance parameter ($\tau = 10^{-1}, 10^{-2}$), the error is lower for most models than expected from interpolation of the smaller tolerances. In line with this, the time steps are not significantly larger than for the next-smaller tolerance tested, especially in the planesource test (see Figure 4.3 for representative plots and Figures A.1 and A.2 in the Appendix). In addition, the time steps oscillate much more. This is due to the fact that the time step predicted from the error estimate is often too large for these tolerances, leading to `infs` and `NaNs` during the computations.

When comparing Figure 4.3 and Figures 4.1(b), 4.2(b), we see that the new scheme is significantly more efficient, at least for long-running tests, as it uses much larger time step to reach the same approximation quality. One might argue that the standard scheme could be similarly efficient when used with an adaptive time stepping scheme. However, finding an adaptive time stepping scheme that (provenly) preserves realizability may be difficult while any time stepping scheme can be used in transformed coordinates.

4.2. Performance

We now compare the performance of the new scheme to the standard splitting scheme. For the standard scheme, we always use $\Delta t = 0.9\Delta t_{max}$, where Δt_{max} is the maximal realizability-preserving timestep given by (3.16). The safety factor 0.9 is included to account for numerical errors during the computation. For

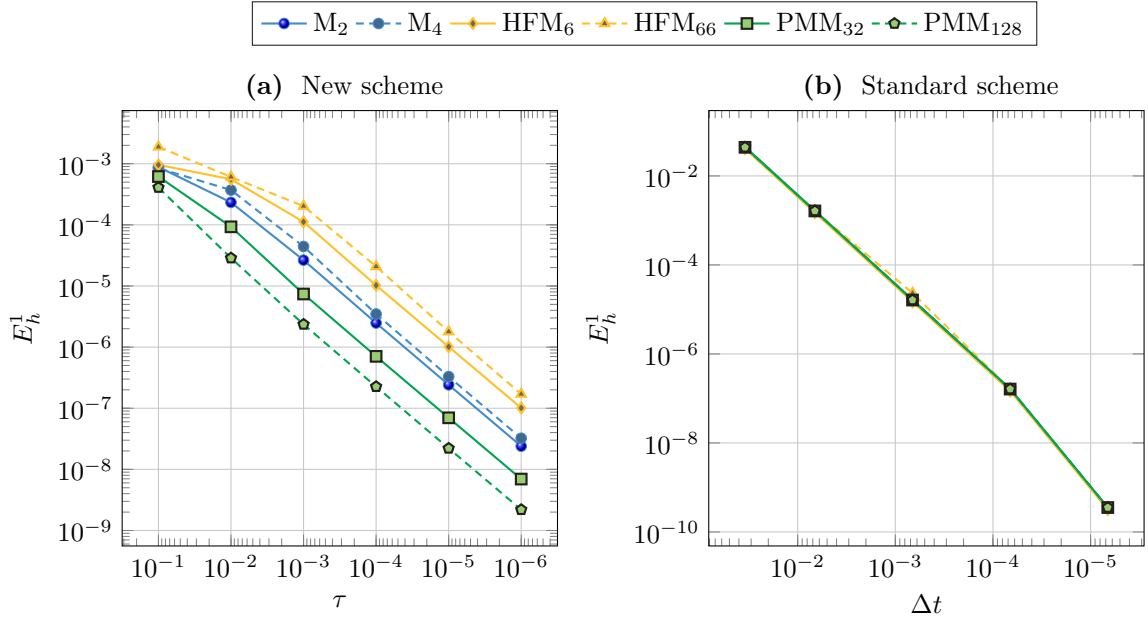


Figure 4.2: L^1 -error against reference solution (new scheme with $\tau = 10^{-9}$) in the pointsource test case ($I = 30^3, t_f = 0.25$). (a) New scheme for decreasing tolerance parameter τ . (b) Standard scheme for decreasing time step Δt .

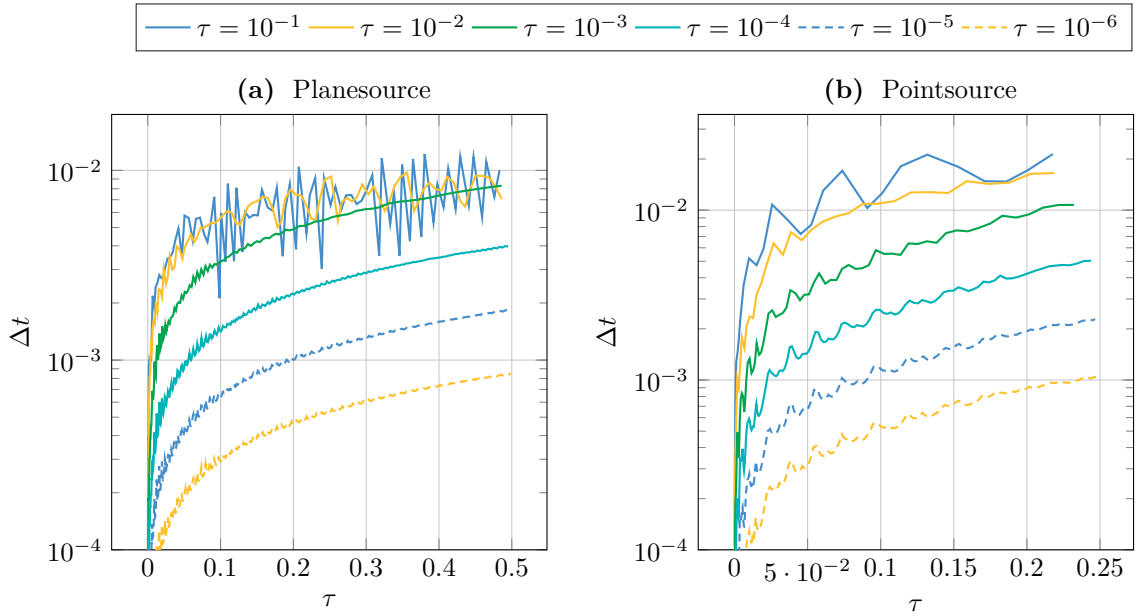


Figure 4.3: Timesteps for the M_{10} model in the planesource test case ($I = 240, t_f = 0.5$) and M_4 model in the pointsource test case ($I = 30^3, t_f = 0.25$) for different tolerance parameters τ . Additional plots can be found in the appendix. The last step has been omitted for all models as it was chosen to reach t_f exactly and thus may be artificially small.

the new scheme, we use a tolerance of $\tau = 10^{-3}$ in slab geometry and $\tau = 10^{-2}$ in three dimensions. As we have seen in the previous subsection 4.1 (see also Tables A.1 and A.2), with these parameters choices the new is often significantly more accurate which is important whenever the time stepping error is of the same order or even larger than the errors due to the spatial discretization and the moment approximation. This seems to be the case, e.g., for the Checkerboard test where the moment approximation errors are relatively small (compare [44]) and for the Shadow test which has a large final time t_f such that time discretization errors accumulate over time. However, for most test cases regarded, the errors introduced by the moment approximation (compare [44]) are much larger than the errors due to the time stepping, even for the standard scheme using Δt_{max} . In general, it would thus not be reasonable to decrease the time step for the standard scheme. Instead, it might be possible to choose larger time steps for the new scheme with an improved error estimate. As seen in the previous section, with the current (standard) error estimate, increasing the tolerance does not improve performance as the time steps are not significantly larger. In some cases, we even observed increased computation times for larger tolerances as time steps had to be recomputed more frequently.

Computational times for the one-dimensional testcases can be found in Figure 4.4. In the planesource test, the new scheme is several times faster than the standard scheme for all models except for the low-order HFM_{*n*} and PMM_{*n*} models. For all models, the time steps are initially very small (about 10^{-11}) but are rapidly increasing (see Figure 4.5(a)). After some time, the time steps are even larger than the time steps taken by the standard scheme for most models. In addition, the time to compute a time step is (on average) much smaller for the new scheme (see 4.6(a)). This is especially true for the M_{*N*} models which is why the speedup for these models is significantly larger than for the HFM_{*n*} and PMM_{*n*} models where solving the optimization problem is already quite fast.

The time needed to compute a timestep is basically constant for the new scheme, except for time steps which have to be recomputed because the error estimate is above the tolerance. In contrast, the time to compute a timestep of the standard scheme is increasing over time. This is probably mostly due to the caching used in the implementation. We use two types of caching. First, for each grid cell we store the moment vector \mathbf{u}_i^{k-1} from the last time step and the corresponding multiplier α_i^{k-1} obtained by entropy minimization. In this way we do not have to solve the optimization problem again if the moment vector in that grid cell did not change during the last time step. In addition, we store the last few solutions of the minimization problem with corresponding input moment vectors per thread of execution, so if several grid cells contain the same values, we only have to perform the optimization once and then use the cached values. In particular, during the first time steps only very few optimization problems have to be solved as most grid cells still contain the initial approximate vacuum. If we encounter a moment vector that can not be found in the caches, we search the moment vector that is closest to the input vector (in one-norm) and use the corresponding multiplier α as an initial guess. The new scheme does not use any caching.

In the Sourcebeam test case, the time steps significantly vary over time for some models (see Figure 4.5(b)). In particular, the M_{*N*} models show strongly oscillating time steps. This is also reflected in the computational times per time step (see Figure 4.6(b)), where frequent recomputations can be observed. The oscillations seem to be much less pronounced for the higher-order models (see Appendix Figures A.3-A.5). As a consequence, computational times for the new scheme are not increasing monotonically with the moment order (see Figure 4.4(b)), e.g., computing the M₂₀ model takes longer than computing the M₆₀ model. Thus, the standard scheme is faster for the low-order models and again significantly slower for the high-order models. Except for the HFM₂ and PMM₂ model, the HFM_{*n*} and PMM_{*n*} models do not show these oscillations and again reach time steps that are larger than Δt_{max} after some time. Consequently, overall computation times are faster with the new scheme.

Similar to the Planesource test in one dimension, the timesteps for the three-dimensional Pointsource and Checkerboard tests are very small initially but increase over time (see Figure 4.8). In the Pointsource test case, the final time $t_f = 0.75$ is relatively small and none of the models reaches Δt_{max} during the test. Consequently, the computation times are only slightly faster for most models with the new scheme (see

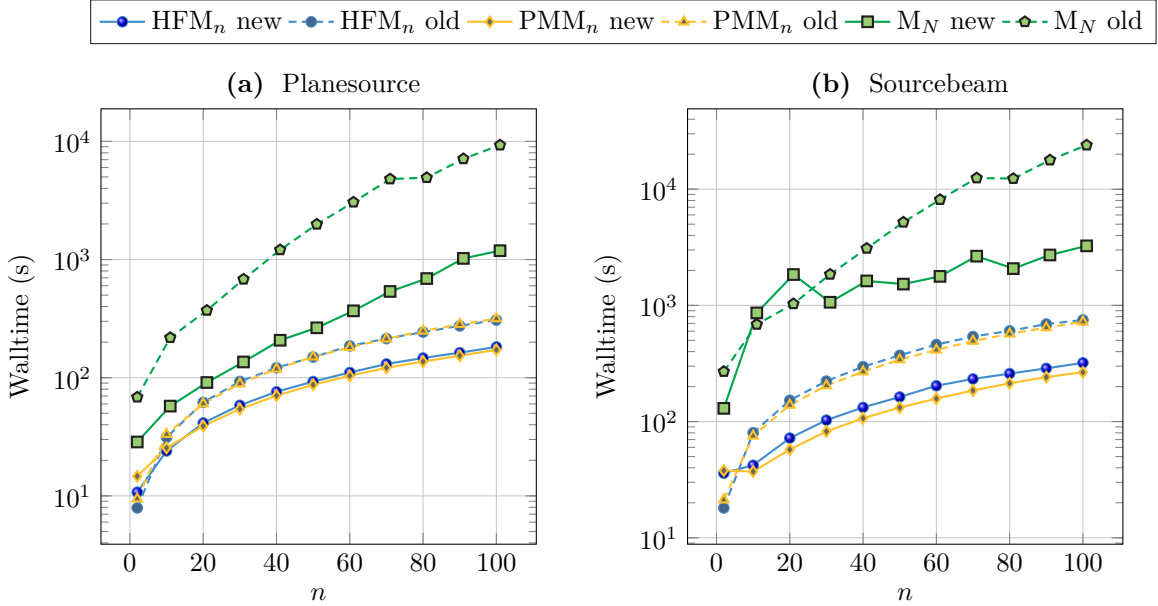


Figure 4.4: Computational times versus moment number n for the two schemes in the one-dimensional tests (1200 grid elements, $\tau = 1e - 3$, no parallelisation). (a) Planesource test case. As expected (see [44], computational times are increasing linearly (HFM $_n$, PMM $_n$) or quadratically (M $_N$). Except for the low-order models, the new scheme is faster than the standard scheme, up to a factor of 10. (b) Sourcebeam test case. For the HFM $_n$ and PMM $_n$ models, results are mostly similar as in the planesource test though the speedup is smaller. The M $_N$ models show an interesting behavior: computing the M $_{10}$ and M $_{20}$ models takes more time with the new scheme, but for higher order models the computational times barely increase.

Figure 4.7(a)). The higher-order PMM $_n$ models show considerably smaller timesteps than the other models and thus overall computation times are even higher than with the standard scheme. The Checkerboard test case has strongly absorbing regions and thus is the first test where the time step restrictions (3.16) and (3.13) significantly differ. After some time, the timesteps are mostly between these two bounds and even exceed the upper bound several times (see Figure 4.8(b)). The higher order M $_N$ models show some oscillations in the beginning but much less than in the Sourcebeam test and the timesteps always stay relatively large. Thus, overall computation times are greatly improved and up to ten times as fast as with the standard splitting scheme. In addition, as mentioned earlier, for this test case the increased accuracy of the new scheme might be important, as the error due to the timestepping with the standard scheme are of the same order as the error due to the spatial and moment approximation. Again, the speedup is smaller for the HFM $_n$ models and non-existent for the PMM $_n$ models.

The Shadow test case is highly challenging for the numerical solvers. In the absorbing domain, very small local particle densities occur, which lead to numerical problems when inverting the Hessians (whose entries scale with the density). In addition, as only right-going particles are entering the domain, densities for particles with negative x -velocity decline much faster than positive x -velocity densities, resulting in very anisotropic distributions and ill-conditioned Hessians. For the standard scheme, we are dealing with these problems by enforcing a minimum density and using an isotropic regularization technique to replace ill-conditioned moment vectors (see Section 3.1). These techniques, in particular the isotropic regularization, introduce additional errors which in theory might completely alter the solution. In practice, regularization is usually mainly applied to moment vectors with very low densities and thus does not destroy accuracy. However, it should be noted that this is not guaranteed automatically and has to be verified for every new application of the scheme. In our case, regularization is massively used by the M $_N$ and PMM $_n$ models. The HFM $_n$ models do not use regularization. For the new scheme, we did not implement a similar regularization technique yet.

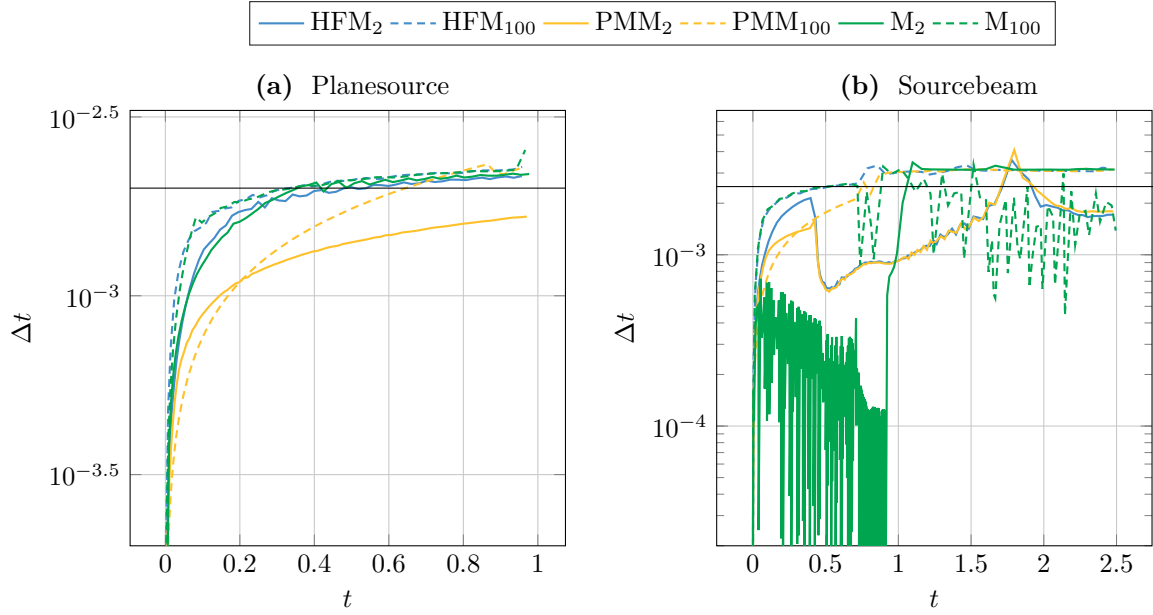


Figure 4.5: Time steps taken in the adaptive Runge-Kutta scheme. For clarity, instead of plotting each time point we plot the mean of 10 time steps each to avoid small oscillations. For both test cases, we use a grid with 1200 elements and a tolerance of $\tau = 1e - 3$ for the time stepping scheme. The solid horizontal line represents the upper bound (3.16) on the time step used in the standard splitting scheme (which approximately agrees with the bound (3.13) because $\frac{1}{\Delta x} \gg \sigma_t$ for these test cases). (a) Planesource test case. The initial time steps are very small (about 10^{-11}) but rapidly increasing. After some time, the time steps are even larger than the time steps taken by the standard scheme for most models. (b) Sourcebeam test case. Other than in the planesource case, the time steps significantly vary over time for some models. In particular, the M_N models show strongly oscillating time steps.

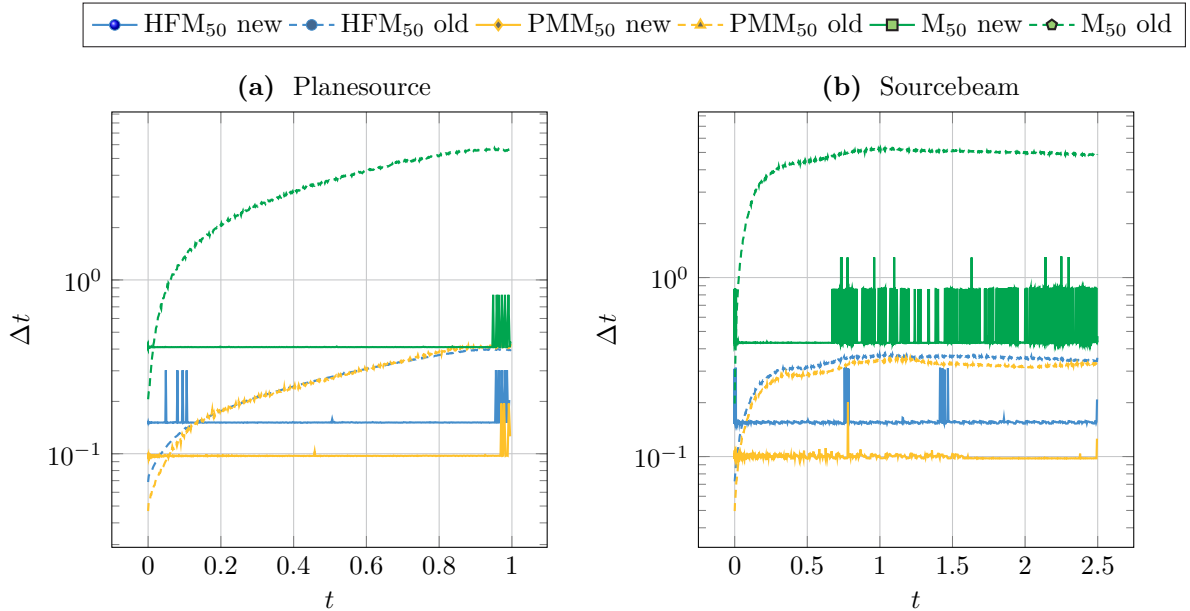


Figure 4.6: Walltimes for computing a single time step. For the standard scheme, the time steps are fast initially and slow down over time. The new scheme takes almost constant time per timestep except for those timesteps that have to be recomputed with a smaller time step length because the error is too high. (a) Planesource test case, $I = 1200$, $t_f = 1$. (b) Sourcebeam test case, $I = 1200$, $t_f = 2.5$.

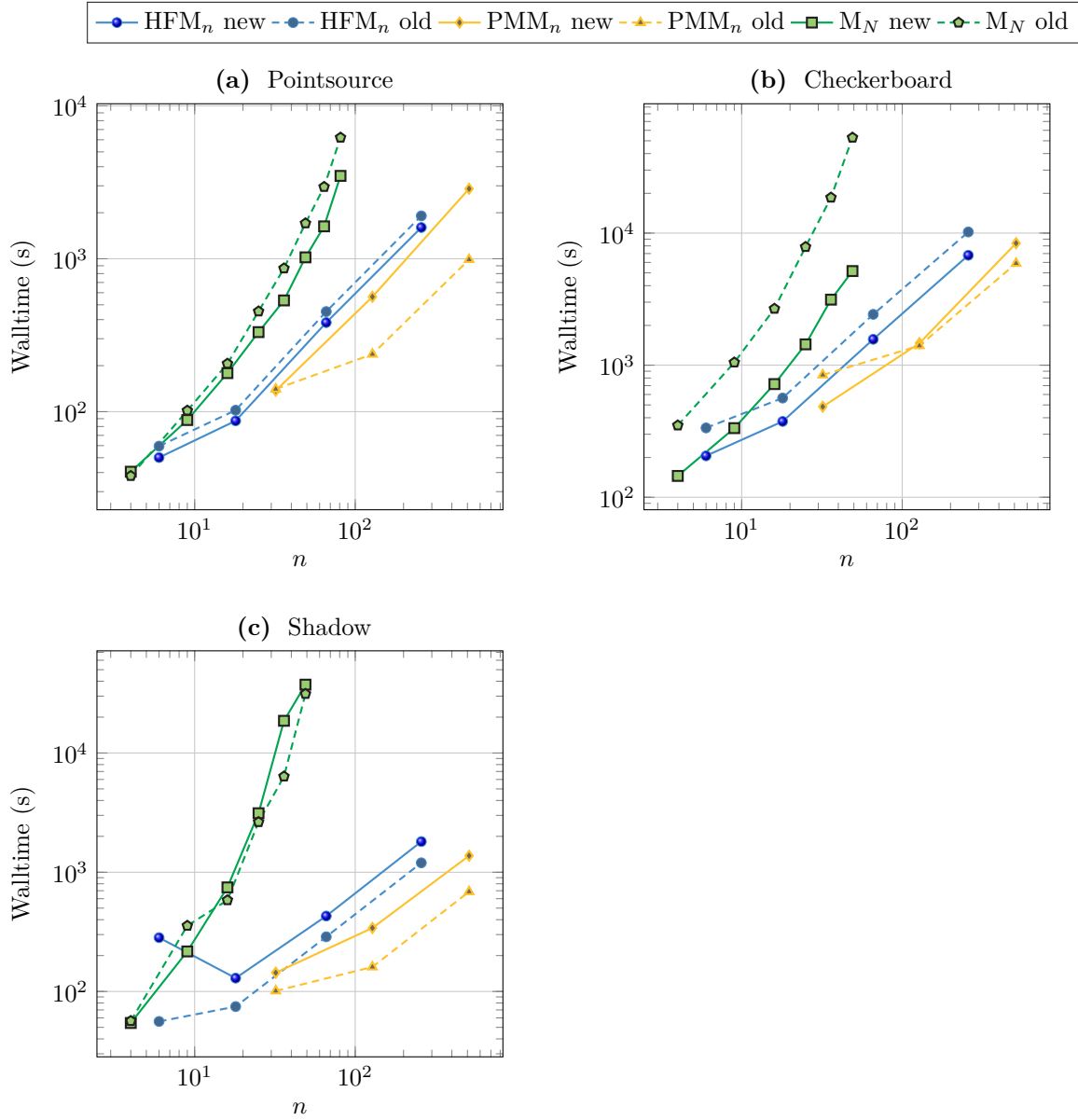


Figure 4.7: Computational times versus moment number n for the two schemes in the three-dimensional tests ($\tau = 1e - 2$, 32 threads, 1000 tasks per thread (compare Section 4.3)). **(a)** Pointsource test case ($I = 50^3$, $t_f = 0.75$). The new scheme is slightly faster for the M_N and HFM_n models and slower for the PMM_n models. **(b)** Checkerboard test case ($I = 70^3$, $t_f = 3.2$). Here, the new scheme is several times faster for the M_N models and slightly faster for the HFM_n models. In the PMM_n tests, the new model is on par or slightly faster in the low-order tests and slightly slower for PMM_{512} . **(c)** Shadow test case ($I = 60 \times 20 \times 15$, $t_f = 20$). The new scheme is significantly slower for the HFM_n and PMM_n models and about as fast as the standard scheme for most M_N models.

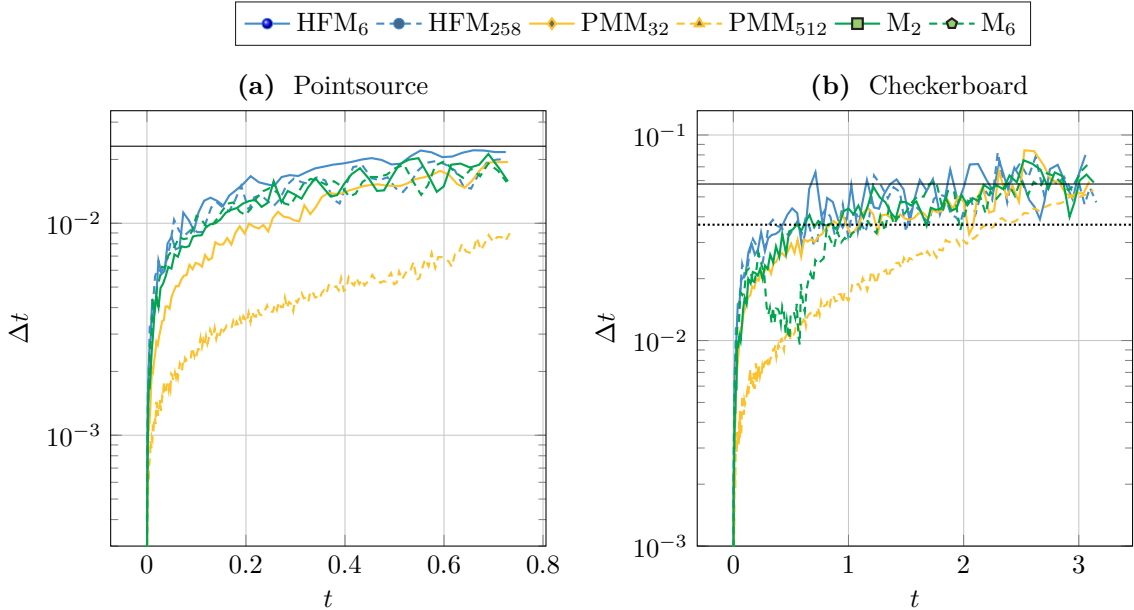


Figure 4.8: Time steps taken in the adaptive Runge-Kutta scheme for a tolerance of $\tau = 1e - 2$. The solid and dotted horizontal line represent the time step restrictions (3.16) and (3.13), respectively (which almost agree for the Pointsource test). **(a)** Pointsource test case with 50^3 grid cells, $t_f = 0.75$. **(b)** Checkerboard test case with 70^3 grid cells, $t_f = 3.2$. For both test cases, the initially small timesteps are approaching the time step length of the standard scheme over time. The PMM₅₁₂ model shows considerably smaller time steps than the other models.

The timesteps for the Shadow test case can be found in Figure 4.10. For the PMM_n models, the higher-order HFM_n models and the M₁ model the timesteps are converging to a value well above the maximum timestep of the unsplit scheme but also significantly below the timestep of the splitting scheme. In addition, computing a timestep for these models is already quite fast with the standard scheme and the speed-up of the new scheme is not large enough to compensate the smaller timestep (see Figure 4.9(c)). Interestingly, the time to compute a timestep with the standard scheme is not monotonically increasing but reaches a maximum at about $t = 5$, probably because the solution reaches a steady state in an increasingly large part of the domain. (see Figure 4.10(a) and Appendix Figures A.7-A.9). As a consequence, computational times are several times higher for the new scheme than for the splitting scheme (see Figure 4.7(c)). Note however that the PMM_n models do not show significant oscillations or other problems though the standard scheme has to use regularization. To be competitive with respect to computation times in this test case, the new scheme probably also needs to use a splitting technique. Though there is no formal limit on the time step for the new scheme due to the strong absorption, we would expect the approximation error (and thus the time step) to be dominated by this term.

The HFM₆ model shows some sharp declines in the time step around $t = 8$ (see Figure 4.10(b)). This is due to the very low density of particles with negative x -velocities which lead to large (in absolute values) negative entries in the α vectors. We tested the following simple regularization technique to solve this problem: Whenever the timestep falls below $\Delta t_{min} = 10^{-2}$, we replace all entries in the α vector that are smaller than $\alpha_{min} = -1000$ by α_{min} . As can be seen in Figure 4.10(c), this removes the very small timesteps. The overall number of timesteps is reduced from 1152 to 547. The L^1 -error between the results with and without regularization is about 10^{-6} . Curiously, the higher-order HFM_n models do not show similar problems.

Though the time steps are considerably smaller than for the standard scheme and highly varying (see Figure 4.10(d) and Appendix Figures A.7-A.9), for the M_N models the new scheme is about as fast as the standard splitting scheme. This is in particular remarkable as the new scheme does not use any regulariza-

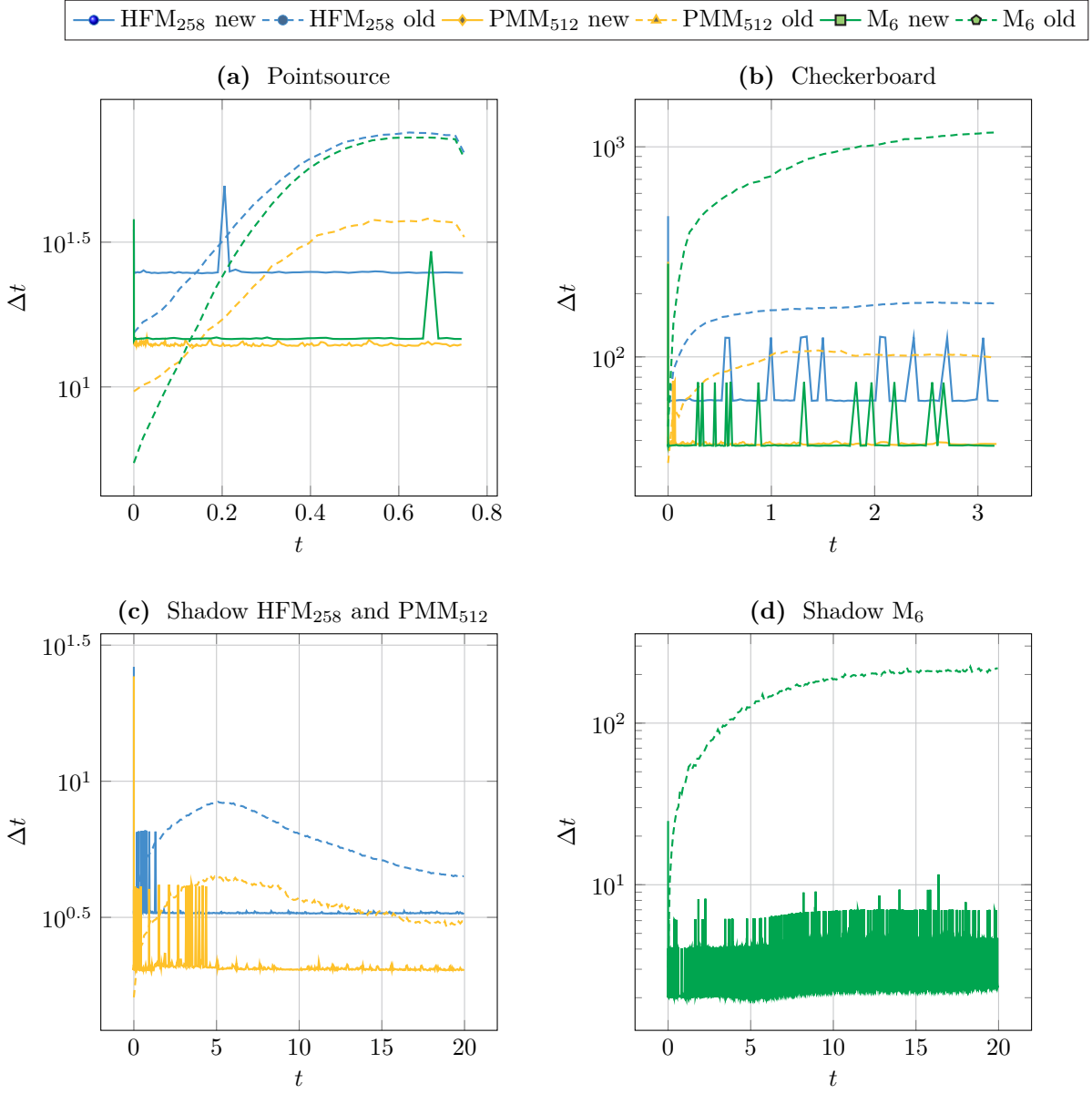


Figure 4.9: Walltimes for computing a single time step. (a) Pointsource test case, $I = 50^3$, $t_f = 0.75$. (b) Checkerboard test case, $I = 70^3$, $t_f = 3.2$. (c) Shadow test case, $I = 60 \times 20 \times 15$, $t_f = 20$, HFM₂₅₈ and PMM₅₁₂. (d) Shadow test case, M₆.

tion. However, frequent recomputations can be observed (see Figure 4.9(d)) indicating a failure of the time step prediction. Curiously, the computational times per timestep of the standard scheme do not decrease for later times as they do for the HFM_n and M_N models. As we still have to invert the Hessians in each grid cell for each time step, we even expected the new scheme to fail at some point as we encounter a very ill-conditioned Hessian that is numerically singular (though the Hessian is guaranteed to be positive definite in exact arithmetic). Though we did not encounter this problem during our tests, it might show up when the scheme is applied to other applications or when higher-order schemes are transformed in the same way. In that case, some regularization technique is needed to replace the multiplier corresponding to the singular Hessian matrix by a multiplier with (numerically) invertible Hessian matrix. Unfortunately, a simple technique as described above for the HFM_n models does not work for the M_N (and PMM_n) models. For the HFM_n models, we know that large negative entries in the vector of multipliers correspond to low densities, as the hat functions are positive. This is not the case for the other bases. We tried to simply replace entries with absolute value above some upper bound by this bound but this introduced large errors and instability to the solutions. Instead, a regularization technique similar to the isotropic regularization (3.17) for the moment vectors can also be used for the multipliers. For regularization parameter $r \in (0, 1]$ as small as possible, replace the multipliers $\boldsymbol{\alpha}$ by the regularized multipliers

$$\boldsymbol{\alpha}^r = \boldsymbol{\alpha}^{r,0} + \ln \frac{\rho(\boldsymbol{\alpha})}{\rho(\boldsymbol{\alpha}_r)} \boldsymbol{\alpha}_{\text{one}} \quad (4.2)$$

where

$$\boldsymbol{\alpha}^{r,0} = (1 - r)\boldsymbol{\alpha} + r\boldsymbol{\alpha}_{\text{iso}}(\rho(\boldsymbol{\alpha})) \quad (4.3)$$

and the second term in (4.2) ensures that the local particle density is not changed by the regularization. Here,

$$\boldsymbol{\alpha}_{\text{iso}}(\rho) = \frac{\rho}{\rho(\langle \mathbf{b} \rangle)} \boldsymbol{\alpha}_{\text{one}} \quad (4.4)$$

are the multipliers corresponding to the isotropic distribution with density ρ .

Using this regularization for some particular ill-conditioned multipliers might also help with erratic time steps observed for the M_N models in the Shadow test case. However, it is not immediately clear how to identify these multipliers and how to decide whether we should reduce the timestep size or use regularization.

4.3. Parallel scaling

As already mentioned, one of the major drawbacks of the minimum entropy based moment models is their computational cost. As we have seen in the previous section, the new scheme often is several times faster than the scheme in standard coordinates. However, even with this speed-up computations without parallelisation still take excessively long. In addition, there are cases where the new scheme is not faster or even slower than the standard scheme.

As the minimization problems or matrix inversions on different grid cells are independent, parallelisation is easily possible for both schemes. However, for the standard scheme, load balancing may be a serious issue [25]. Usually, some minimization problems are harder to solve than others, resulting in different numbers of iterations in the Newton scheme. The new scheme does not have this problem, as it only needs the inversion of a relatively small positive definite matrix in each grid cell. For these matrix sizes, direct solvers usually perform at least as good as iterative methods and take an approximately constant time per inversion.

To investigate the scaling behavior, for both schemes we computed ten time steps of the pointsource test case with a varying number of threads. We use a work-stealing task-based parallelisation (implemented using Intel TBB [23]). To see the impact of load balancing we perform all test both with 1 task per thread (no load balancing) and 1000 tasks per thread. The results are shown in Figure 4.11. If load balancing is

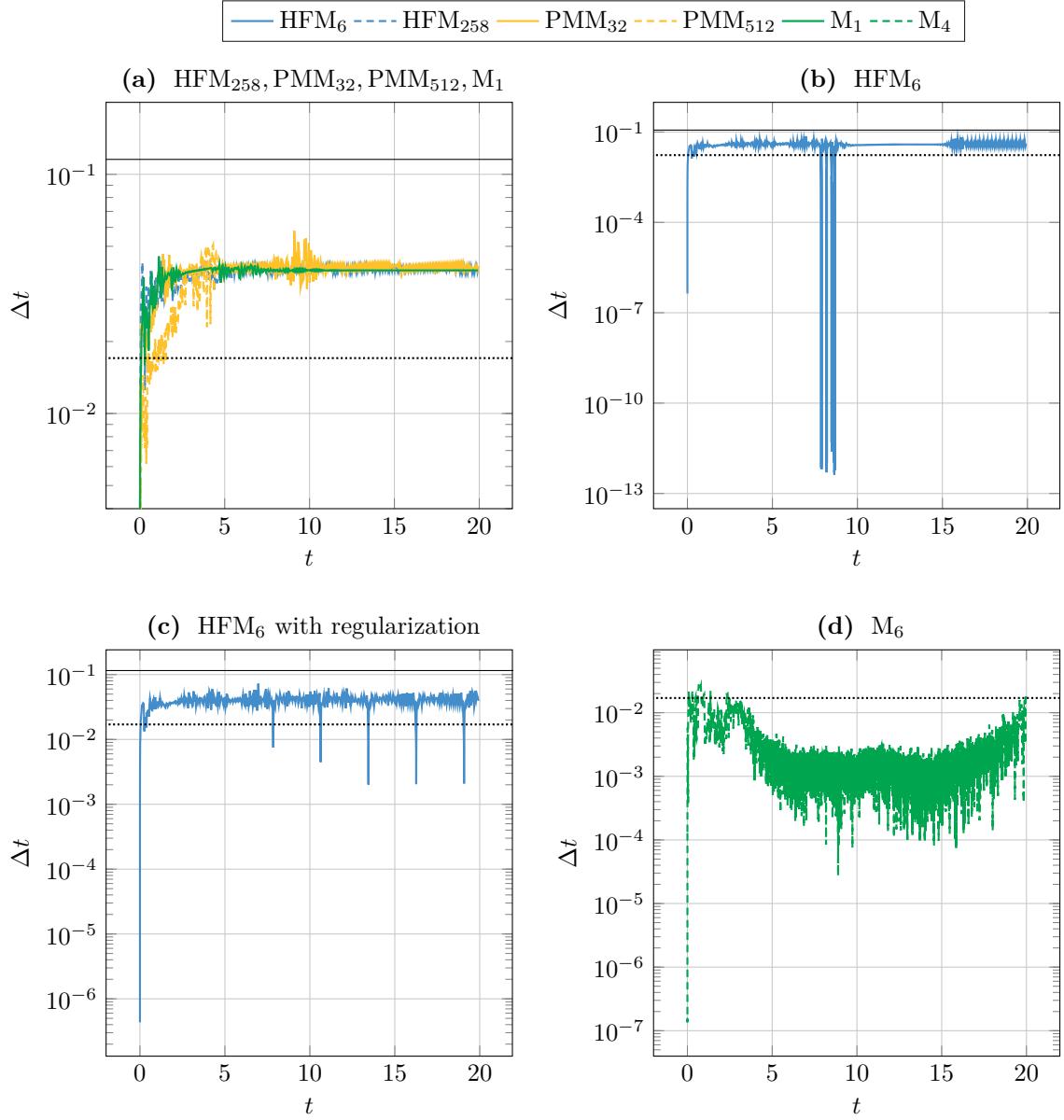


Figure 4.10: Time steps taken by the adaptive Runge-Kutta scheme in the Shadow testcase ($I = 60 \times 20 \times 15$, $t_f = 20$) for a tolerance of $\tau = 1e-2$. The solid and dotted horizontal line represent the time step restrictions (3.16) and (3.13), respectively. (a) The M_1 , PMM_n and higher-order HFM_n models show very few oscillations and converge to a common timestep. (b) For the HFM_6 , the time step sharply declines around $t = 8$. (c) When enforcing a lower bound of -1000 on the entries of the multipliers α , the time steps stay above 10^{-3} . (d) The higher-order M_N models show significant oscillations and smaller timesteps than the other models.

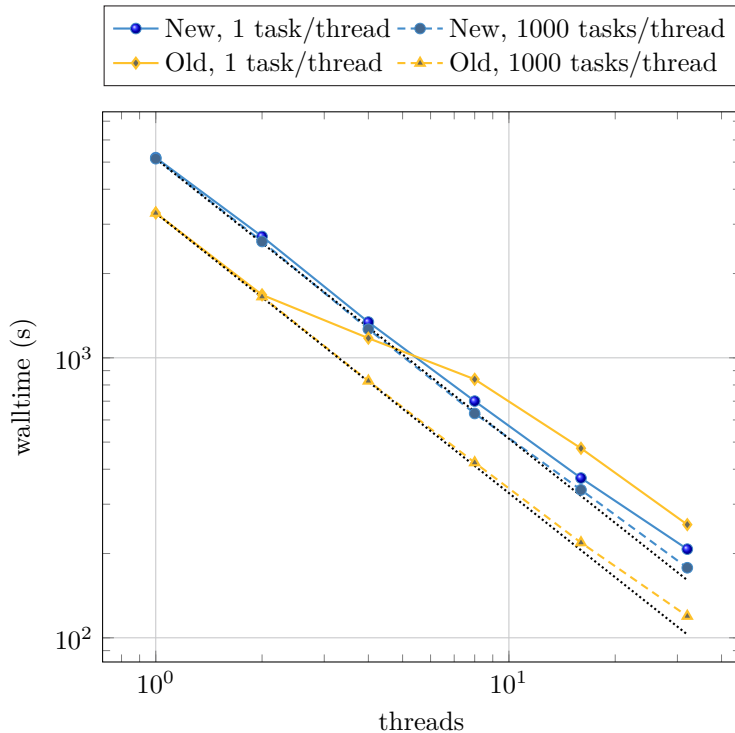


Figure 4.11: Computational times for 10 time steps in the pointsource test ($I = 100^3$, M_3 model) against number of threads. The dotted lines represent perfect scaling.

used, both schemes scale almost perfectly to 16 threads. When going to 32 threads the scaling is slightly worse which may be due to the used dual-socket system with 2×16 cpu cores.

Removing the load balancing has a large impact on the standard scheme while the new scheme is much less affected. We would expect that this difference is emphasized if even more threads (or processes) are used. The new scheme thus should be better suited to massively (MPI)-parallel computations.

4.4. Masslumping

The basis functions used by the HFM_n models are basically the Lagrange \mathbb{P}_1 nodal basis functions used in the (continuous) finite element method, i.e., each basis function evaluates to 1 on exactly one node of the triangulation and to 0 on all other nodes (see Section 2.3). As a consequence, the Hessian matrix 3.18 is tridiagonal (in one dimension) or sparse (three dimensions). Compared to the M_N models where the Hessian is dense, this significantly reduces the computational effort required for assembly and inversion. However, especially in three dimensions, assembling and inverting the Hessian matrix still account for the vast majority of the computational time.

We can significantly speed up these computations by using a quadrature that only contains the nodes of the triangulation. With such a quadrature, the basis functions always evaluate to either 1 or 0 and the Hessian matrix becomes diagonal. The downside is, of course, that an additional quadrature error is introduced as the nodal quadrature is only of first order. However, this additional error is of the same order as introduced by the linear finite element discretization. This approach is sometimes called masslumping as using such a quadrature diagonalizes the mass matrix in the finite element method (“all mass is lumped together on the diagonal”).

For the one-dimensional tests, we use the two-point Gauss-Lobatto quadrature in each interval (containing

only the end-points of interval) for the masslumped version. As quadrature points that are on the same vertex of the partitioning can be merged, we only have one quadrature point per vertex. The reference quadrature uses 24 quadrature points per interval. In addition, we only have to evaluate one component of the integrand per quadrature point (the one corresponding to the non-zero basis function) instead of two. Overall, this reduces the number of integrand evaluations by a factor of about 48. The results can be found in Figure 4.12. For both test cases, almost independently of the number of moments n , the computations are about 40 times as fast using masslumping (see Figure 4.12(a)). This is in line with the reduction in the number of quadrature points. The L^1 errors (compared to the non-masslumped result) are decreasing with second order (see Figure 4.12(b)). The L^∞ errors in the sourcebeam test are decreasing with order about 1.3, while the L^∞ in the planesource tests are converging with very low order.

For the three-dimensional tests, we use the vertex quadrature on the reference triangle (with the vertexes $(0,0)$, $(1,0)$, $(0,1)$ as quadrature points and weight $\frac{1}{6}$ each) transferred to each spherical triangle. This results in one quadrature point per vertex of the triangulation. The triangulation consists of $2 \cdot 4^{r+1}$ triangles and $2 + 4^{r+1}$ vertices [44] (where r is the number of refinements of the initial octants), and the reference quadrature has 55 quadrature points per spherical triangle. The standard implementation thus uses about 110 times as many evaluations. The results can be found in Figure 4.13. For all test cases, the masslumped version is more than two orders of magnitude faster than the version using the reference quadrature. The maximum speed-up is 216 times (Pointsource, HFM₁₀₂₆), which is considerably higher than the reduction in quadrature points. The additional speed-up is due to the more efficient implementation, as the masslumped version does not need to use sparse matrices and the associated indirect indexing. When looking at the profiler results, we see that the time for assembling and inverting the (diagonal) Hessian is negligible in the masslumped version. Overall, the time needed for the operator evaluation (which consists of calculating the kinetic fluxes and the source term and applying the inverse Hessian matrix) has been reduced to a point where the vector operations in the adaptive Runge-Kutta scheme now make up a major part of the computation time.

For all testcases, the errors compared to the non-masslumped version are quite large (see Figure 4.13(b)). However, both the L^1 and the L^∞ error converge with first order in n for all testcases which corresponds to second order convergence in the grid width of the (velocity space) triangulation, as each refinement halves the grid width but increases the number of vertices (approximately) by a factor of 4. The convergence rate thus is similar (for the Checkerboard test) to or even higher (Pointsource, Shadow) than the convergence of the (second-order discretization of the) moment approximation (compare [44]). Thus, for high-order models, the additional quadrature error introduced by masslumping might be acceptable given the massive speed-up. In any case, it might be preferable to replace a lower-order moment model with high-order quadrature by a higher-order masslumped model.

5. Conclusion and outlook

In this paper, we introduced a new numerical scheme for entropy-based moment equations that is based on a coordinate transformation of the semi-discretized equations and gets rid of the minimum-entropy optimization problems (except for the initial values). We have shown analytically and numerically that the new scheme converges to the correct solutions. In addition, we investigated the performance of the new scheme in several numerical benchmarks and showed that it is often several times faster than the untransformed scheme, at the same or even higher accuracy in time. In addition, for the hatfunction basis, we showed that a massive speed-up can be obtained by using a quadrature that contains only the vertices of the triangulation (at the cost of additional quadrature error), making very high-order models computable in reasonable time. Finally, we did some tests on parallel scaling of the schemes which suggest that the new scheme does not have the same load-balancing problems as the untransformed scheme.

To improve the scheme, better error estimates for the adaptive timesteppers should be investigated to get rid of the erratic time step behavior observed in the Sourcebeam and Shadow tests. Here, larger errors could be

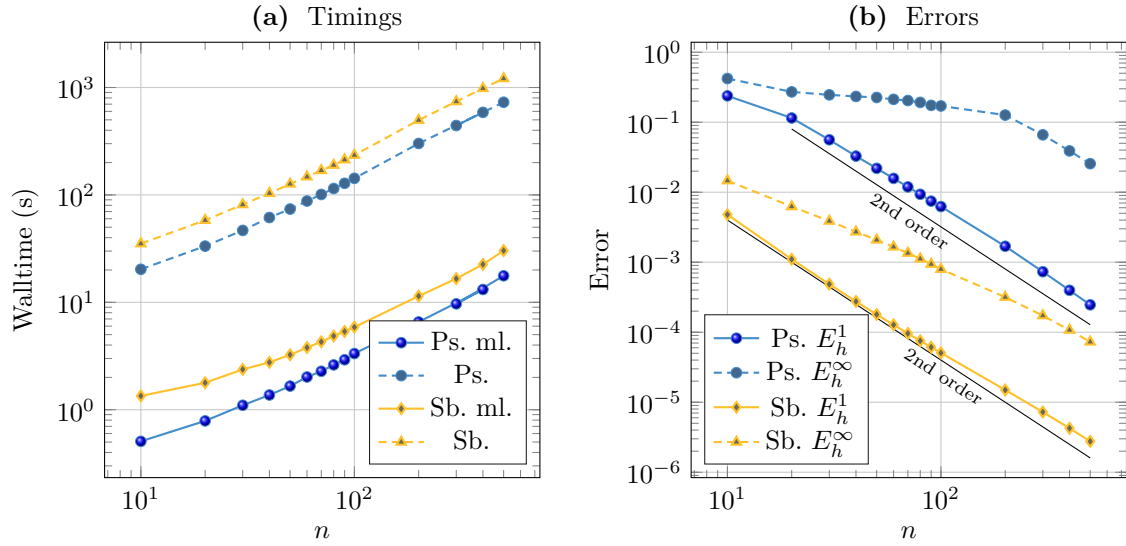


Figure 4.12: Effect of masslumping on computational times and accuracy of the HFM_n models in the one-dimensional tests (1200 grid elements, $\tau = 1e-3$, no parallelisation). Ps: Planesource, Sb: Sourcebeam, ml: masslumped. (a) Computational times versus moment number. (b) Errors introduced by masslumping (reference is the non-masslumped solution).

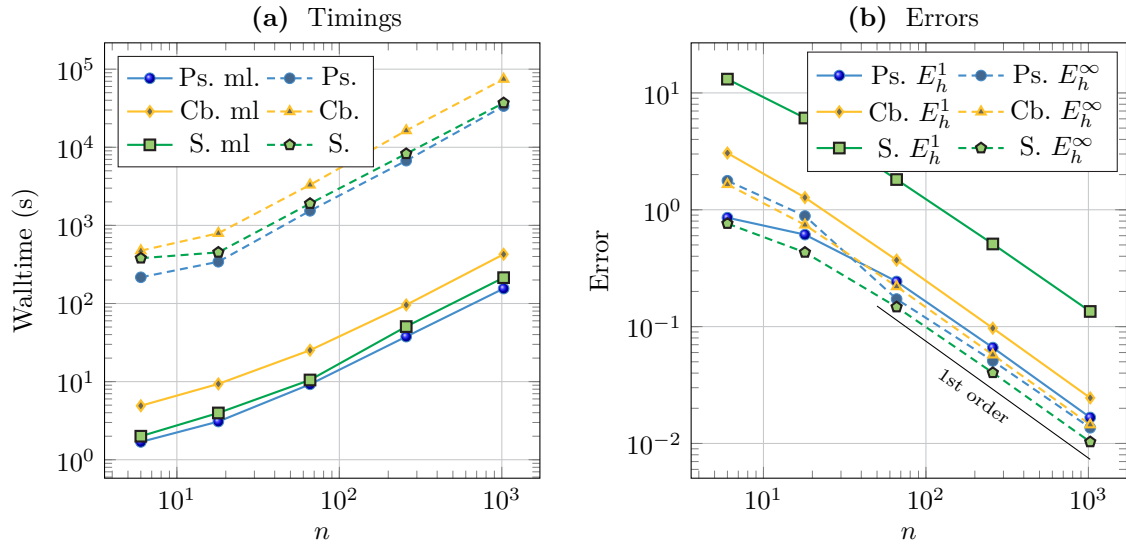


Figure 4.13: Effect of masslumping on computational times and accuracy of the HFM_n models in the three-dimensional tests ($\tau = 1e-2$, no parallelisation). Ps: Pointsource ($I = 30^3$, $t_f = 0.75$), Cb: Checkerboard ($I = 35^3$, $t_f = 3.2$), S: Shadow ($I = 36 \times 12 \times 9$, $t_f = 20$), ml: masslumped. (a) Computational times versus moment number. (b) Errors introduced by masslumping (reference is the non-masslumped solution).

allowed for multipliers that correspond to small densities and thus only have a minor effect on the solution in original coordinates. In addition, regularization techniques could be used to replace such multipliers if they limit the time step. These regularization techniques might also be needed to be able to solve problems where some Hessians are numerically singular. For applications involving strong scattering or absorption, splitting methods for the new scheme might be of interest to remove the time step restriction induced by the corresponding terms.

While we restricted ourselves to a first-order scheme, the same coordinate transformation can also be applied to higher-order kinetic schemes as regarded, e.g., in [41, 43].

In future work, we will investigate further model reduction by POD-based reduced basis methods [22, 34] which should be much easier with the new scheme as it is well-defined on the whole \mathbb{R}^n and not only on the realizable set (which is a convex cone in \mathbb{R}^n).

Acknowledgments

The authors thank Florian Schneider for fruitful discussions.

References

- [1] G. ALLDREDGE AND F. SCHNEIDER, *A realizability-preserving discontinuous Galerkin scheme for entropy-based moment closures for linear kinetic equations in one space dimension*, Journal of Computational Physics, 295 (2015), pp. 665–684, <https://doi.org/10.1016/j.jcp.2015.04.034>.
- [2] G. W. ALLDREDGE, M. FRANK, AND C. D. HAUCK, *A regularized entropy-based moment method for kinetic equations*, SIAM Journal on Applied Mathematics, 79 (2019), pp. 1627–1653, <https://doi.org/10.1137/18m1181201>.
- [3] G. W. ALLDREDGE, C. D. HAUCK, D. P. O’LEARY, AND A. L. TITS, *Adaptive change of basis in entropy-based moment closures for linear kinetic equations*, Journal of Computational Physics, 258 (2014), pp. 489–508, <https://doi.org/10.1016/j.jcp.2013.10.049>.
- [4] G. W. ALLDREDGE, C. D. HAUCK, AND A. L. TITS, *High-order entropy-based closures for linear transport in slab geometry II: A computational study of the optimization problem*, SIAM Journal on Scientific Computing, 34 (2012), pp. B361–B391, <https://doi.org/10.1137/11084772X>.
- [5] P. BOGACKI AND L. F. SHAMPINE, *A 3(2) pair of Runge-Kutta formulas*, Applied Mathematics Letters. An International Journal of Rapid Publication, 2 (1989), pp. 321–325, [https://doi.org/10.1016/0893-9659\(89\)90079-7](https://doi.org/10.1016/0893-9659(89)90079-7).
- [6] L. BOLTZMANN, *Weitere studien über das wärmegleichgewicht unter gasmolekülen*, Sitzungsberichte der Akademie der Wissenschaften, Mathematische-Naturwissenschaftliche Klasse, 66 (1872), pp. 275–370.
- [7] R. BORSCHKE, A. KLAR, AND F. SCHNEIDER, *Kinetic and moment models for cell motion in fiber structures*, in Active particles, Vol. 2, Model. Simul. Sci. Eng. Technol., Birkhäuser/Springer, Cham, 2019, pp. 1–38.
- [8] T. A. BRUNNER AND J. P. HOLLOWAY, *Two-dimensional time dependent Riemann solvers for neutron transport*, Journal of Computational Physics, 210 (2005), pp. 386–399, <https://doi.org/10.1016/j.jcp.2005.04.011>.
- [9] C. CERCIGNANI, *The Boltzmann Equation and Its Applications*, vol. 67 of Applied Mathematical Sciences, Springer New York, New York, NY, 1988.
- [10] P. CHIDYAGWAI, M. FRANK, F. SCHNEIDER, AND B. SEIBOLD, *A Comparative Study of Limiting Strategies in Discontinuous Galerkin Schemes for the M_1 Model of Radiation Transport*, Journal of Computational and Applied Mathematics, 342 (2018), pp. 399–418, <http://arxiv.org/abs/1706.10174>.
- [11] R. E. CURTO AND L. A. FIALKOW, *Recursiveness, positivity, and truncated moment problems*, Houston Journal of Mathematics, 17 (1991), pp. 603–635.
- [12] B. DUBROCA AND J.-L. FEUGEAS, *Entropic Moment Closure Hierarchy for the Radiative Transfer Equation*, C. R. Acad. Sci. Paris Ser. I, 329 (1999), pp. 915–920.
- [13] B. DUBROCA AND A. KLAR, *Half-moment closure for radiative transfer equations*, Journal of Computational Physics, 180 (2002), pp. 584–596, <http://www.sciencedirect.com/science/article/pii/S0021999102971068>.
- [14] M. FRANK, B. DUBROCA, AND A. KLAR, *Partial moment entropy approximation to radiative heat transfer*, Journal of Computational Physics, 218 (2006), pp. 1–18, <http://www.sciencedirect.com/science/article/pii/S002199910600057X>.
- [15] K. O. FRIEDRICHS AND P. D. LAX, *Systems of conservation equations with a convex extension.*, Proceedings of the National Academy of Sciences of the United States of America, 68 (1971), pp. 1686–1688, <https://doi.org/10.1073/pnas.68.8.1686>.
- [16] B. D. GANAPOL, R. S. BAKER, J. A. DAHL, AND R. E. ALCOUFFE, *Homogeneous infinite media time-dependent analytical benchmarks*, tech. report, Tech. Rep. LA-UR-01-1854. Los Alamos National Laboratory, 2001.

- [17] S. GOTTLIEB, *On High Order Strong Stability Preserving RungeKutta and Multi Step Time Discretizations*, Journal of Scientific Computing, 25 (2005), pp. 105–128, <https://doi.org/10.1007/s10915-004-4635-5>, <http://link.springer.com/10.1007/s10915-004-4635-5>.
- [18] K. P. HADELER, *Reaction transport systems in biological modelling*, in Mathematics Inspired by Biology, V. Capasso, ed., Lecture Notes in Mathematics, Springer Berlin Heidelberg, 1999, <https://doi.org/10.1007/BFb0092373>.
- [19] E. HAIRER, G. WANNER, AND S. P. NØRSETT, *Solving Ordinary Differential Equations I: Nonstiff Problems*, vol. 8 of Springer Series in Computational Mathematics, Springer-Verlag Berlin Heidelberg, second revised edition ed., 1993.
- [20] C. D. HAUCK, *High-order entropy-based closures for linear transport in slab geometry*, Commun. Math. Sci. v9, (2010), http://www.ki-net.umd.edu/pubs/files/FRG-2010-Hauck-Cory.entropy_kinetic.pdf.
- [21] T. HILLEN AND K. J. PAINTER, *Transport and anisotropic diffusion models for movement in oriented habitats*, in Dispersal, Individual Movement and Spatial Ecology, M. A. Lewis, P. K. Maini, and S. V. Petrovskii, eds., vol. 2071 of Lecture Notes in Mathematics, Springer Berlin Heidelberg, Berlin, Heidelberg, 2013, pp. 177–222, https://doi.org/10.1007/978-3-642-35497-7_7.
- [22] C. HIMPE, T. LEIBNER, AND S. RAVE, *Hierarchical approximate proper orthogonal decomposition*, SIAM Journal on Scientific Computing, 40 (2018), pp. A3267–A3292, <https://doi.org/10.1137/16M1085413>.
- [23] INTEL, *Threading building blocks*, <https://software.intel.com/en-us/tbb>.
- [24] M. JUNK, *Maximum entropy for reduced moment problems*, Mathematical Models and Methods in Applied Sciences, 10 (2000), pp. 1001–1025, <https://doi.org/10.1142/S0218202500000513>.
- [25] C. KRISTOPHER GARRETT, C. HAUCK, AND J. HILL, *Optimization and large scale computation of an entropy-based moment closure*, Journal of Computational Physics, 302 (2015), pp. 573–590, <https://doi.org/10.1016/j.jcp.2015.09.008>.
- [26] K. LANCKAU, *Cercignani, c., the Boltzmann equation and its applications.*, ZAMM - Journal of Applied Mathematics and Mechanics / Zeitschrift für Angewandte Mathematik und Mechanik, 69 (1989), p. 423, <https://doi.org/10.1002/zamm.19890691125>.
- [27] C. D. LEVERMORE, *Moment closure hierarchies for kinetic theories*, Journal of Statistical Physics, 83 (1996), pp. 1021–1065, <https://doi.org/10.1007/BF02179552>.
- [28] E. E. LEWIS AND W. F. MILLER, JR., *Computational Methods in Neutron Transport*, John Wiley and Sons, New York, 1984.
- [29] P. A. MARKOWICH, C. A. RINGHOFER, AND C. SCHMEISER, *Semiconductor equations*, Springer-Verlag, Vienna, 1990, <https://doi.org/10.1007/978-3-7091-6961-2>.
- [30] D. MIHALAS AND B. WEIBEL-MIHALAS, *Foundations of radiation hydrodynamics*, Dover, 1999.
- [31] G. MINERBO, *Ment: A maximum entropy algorithm for reconstructing a source from projection data*, Computer Graphics and Image Processing, 10 (1979), pp. 48–68.
- [32] G. N. MINERBO, *Maximum entropy Eddington factors*, J. Quant. Spectrosc. Radiat. Transfer, 20 (1978), pp. 541–545.
- [33] E. OLBRANT, C. D. HAUCK, AND M. FRANK, *A realizability-preserving discontinuous Galerkin method for the M1 model of radiative transfer*, Journal of Computational Physics, 231 (2012), pp. 5612–5639, <https://doi.org/10.1016/j.jcp.2012.03.002>.
- [34] A. QUARTERONI, A. MANZONI, AND F. NEGRI, *Reduced basis methods for partial differential equations*, vol. 92 of Unitext, Springer, Cham, 2016, <https://doi.org/10.1007/978-3-319-15431-2>. An introduction, La Matematica per il 3+2.
- [35] J. RITTER, A. KLAR, AND F. SCHNEIDER, *Partial-moment minimum-entropy models for kinetic chemotaxis equations in one and two dimensions*, Journal of Computational and Applied Mathematics, 306 (2016), pp. 300–315, <https://doi.org/10.1016/j.cam.2016.04.019>.
- [36] R. P. SCHAEERER, P. BANSAL, AND M. TORRILHON, *Efficient algorithms and implementations of entropy-based moment closures for rarefied gases*, Journal of Computational Physics, 340 (2017), pp. 138–159, <https://doi.org/10.1016/j.jcp.2017.02.064>.
- [37] C. SCHÄR AND P. K. SMOLARKIEWICZ, *A Synchronous and Iterative Flux-Correction Formalism for Coupled Transport Equations*, Journal of Computational Physics, 128 (1996), pp. 101–120, <https://doi.org/10.1006/jcph.1996.0198>.
- [38] F. SCHNEIDER, *First-order quarter- and mixed-moment realizability theory and Kershaw closures for a Fokker-Planck equation in two space dimensions: Code*, 2016, <https://doi.org/10.5281/zenodo.48753>.
- [39] F. SCHNEIDER, *Implicit-explicit, realizability-preserving first-order scheme for moment models with lipschitz-continuous source terms*, arXiv:1611.01314, (2016).
- [40] F. SCHNEIDER, *Kershaw closures for linear transport equations in slab geometry II: high-order realizability-preserving discontinuous-Galerkin schemes*, Journal of Computational Physics, 322 (2016), pp. 920–935, <https://doi.org/10.1016/j.jcp.2016.07.014>.
- [41] F. SCHNEIDER, *Moment models in radiation transport equations*, Verlag Dr. Hut, 2016.
- [42] F. SCHNEIDER, G. W. ALLDREDGE, M. FRANK, AND A. KLAR, *Higher Order Mixed-Moment Approximations for the Fokker-Planck Equation in One Space Dimension*, SIAM Journal on Applied Mathematics, 74 (2014), pp. 1087–1114, <https://doi.org/10.1137/130934210>.
- [43] F. SCHNEIDER, G. W. ALLDREDGE, AND J. KALL, *A realizability-preserving high-order kinetic scheme using weno reconstruction for entropy-based moment closures of linear kinetic equations in slab geometry*, Kinetic & Related Models, 9 (2016), p. 193, <https://doi.org/10.3934/krm.2016.9.193>.
- [44] F. SCHNEIDER AND T. LEIBNER, *First-order continuous- and discontinuous-galerkin moment models for a linear kinetic equation: realizability-preserving splitting scheme and numerical analysis*, arXiv e-prints, (2019), arXiv:1904.03098, <https://arxiv.org/abs/1904.03098>.
- [45] F. SCHNEIDER AND T. LEIBNER, *First-order continuous- and discontinuous-galerkin moment models for a linear kinetic equation: Model derivation and realizability theory*, Journal of Computational Physics, 416 (2020),

- p. 109547, <https://doi.org/https://doi.org/10.1016/j.jcp.2020.109547>, <http://www.sciencedirect.com/science/article/pii/S0021999120303211>.
- [46] F. SCHNEIDER, A. ROTH, AND J. KALL, *First-order quarter- and mixed-moment realizability theory and Kershaw closures for a Fokker-Planck equation in two space dimensions*, *Kinetic and Related Models*, 10 (2017), pp. 1127–1161, <https://doi.org/10.3934/krm.2017044>.
- [47] B. SEIBOLD AND M. FRANK, *StaRMAP—A Second Order Staggered Grid Method for Spherical Harmonics Moment Equations of Radiative Transfer*, *ACM Transactions on Mathematical Software*, 41 (2014), pp. 1–28, <https://doi.org/10.1145/2590808>.
- [48] X. ZHANG AND C. W. SHU, *On positivity-preserving high order discontinuous Galerkin schemes for compressible Euler equations on rectangular meshes*, *Journal of Computational Physics*, 229 (2010), pp. 8918–8934, <https://doi.org/10.1016/j.jcp.2010.08.016>.

Appendix A. Appendix

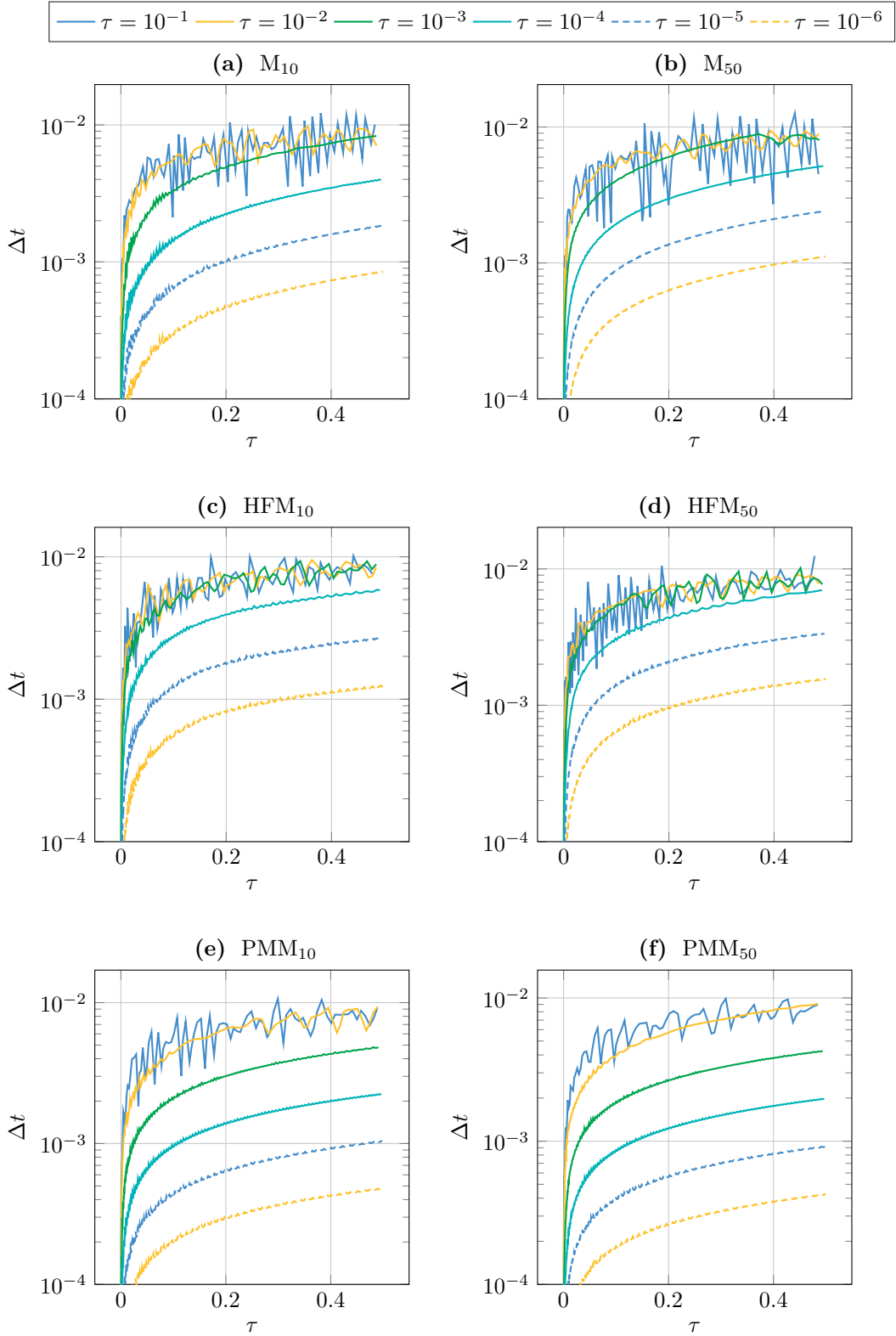


Figure A.1: Timesteps taken in the planesource test case ($I = 240$, $t_f = 0.5$) for different tolerance parameters τ . The last step has been omitted for all models as it was chosen to reach t_f exactly and thus may be artificially small.

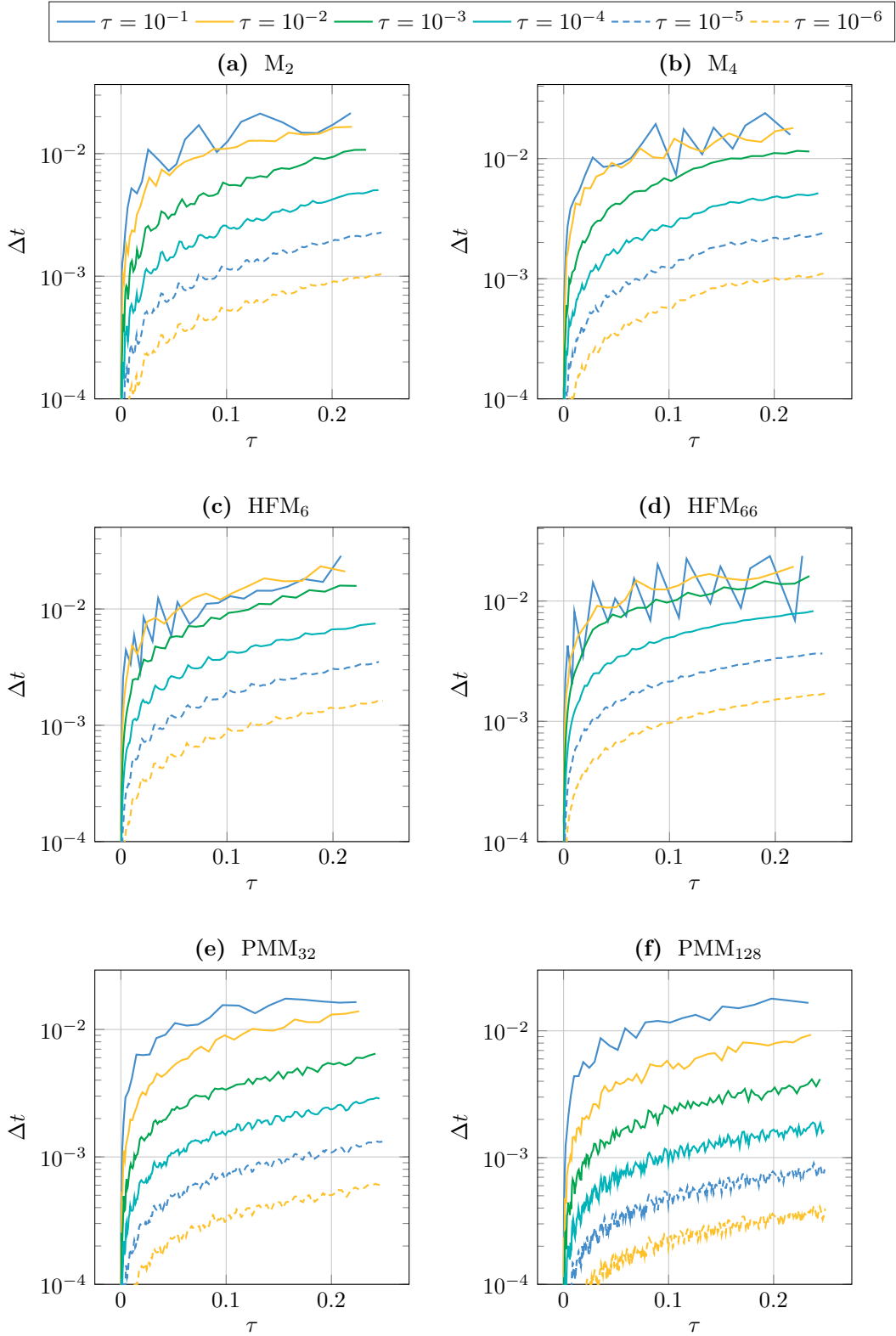


Figure A.2: Timesteps taken in the pointsource test case ($I = 30^3$, $t_f = 0.25$) for different tolerance parameters τ . The last step has been omitted for all models as it was chosen to reach t_f exactly and thus may be artificially small.

Testcase	I	t_f	Model	Scheme	Δt	τ	E_h^1	E_h^∞
Planesource	1200	1	HFM ₂	new	—	1e-03	1.47e-04	1.63e-04
Planesource	1200	1	HFM ₂	old	0.001800	—	4.24e-03	9.33e-03
Planesource	1200	1	HFM ₁₀	new	—	1e-03	2.89e-04	1.97e-04
Planesource	1200	1	HFM ₁₀	old	0.001800	—	4.27e-03	5.69e-03
Planesource	1200	1	HFM ₅₀	new	—	1e-03	2.40e-04	1.07e-04
Planesource	1200	1	HFM ₅₀	old	0.001800	—	2.79e-04	9.40e-04
Planesource	1200	1	HFM ₁₀₀	new	—	1e-03	2.43e-04	1.07e-04
Planesource	1200	1	HFM ₁₀₀	old	0.001800	—	2.61e-04	9.42e-04
Planesource	1200	1	PMM ₂	new	—	1e-03	8.80e-05	9.68e-05
Planesource	1200	1	PMM ₂	old	0.001800	—	4.24e-03	9.33e-03
Planesource	1200	1	PMM ₁₀	new	—	1e-03	2.83e-05	5.52e-05
Planesource	1200	1	PMM ₁₀	old	0.001800	—	3.94e-03	5.53e-03
Planesource	1200	1	PMM ₅₀	new	—	1e-03	1.66e-05	1.38e-05
Planesource	1200	1	PMM ₅₀	old	0.001800	—	4.42e-04	8.76e-04
Planesource	1200	1	PMM ₁₀₀	new	—	1e-03	1.55e-05	1.23e-05
Planesource	1200	1	PMM ₁₀₀	old	0.001800	—	2.65e-04	9.40e-04
Planesource	1200	1	M ₁	new	—	1e-03	8.79e-05	9.67e-05
Planesource	1200	1	M ₁	old	0.001800	—	4.24e-03	9.33e-03
Planesource	1200	1	M ₁₀	new	—	1e-03	3.00e-05	3.77e-05
Planesource	1200	1	M ₁₀	old	0.001800	—	4.61e-03	4.58e-03
Planesource	1200	1	M ₅₀	new	—	1e-03	4.61e-05	3.63e-05
Planesource	1200	1	M ₅₀	old	0.001800	—	3.22e-04	9.43e-04
Planesource	1200	1	M ₁₀₀	new	—	1e-03	5.13e-05	3.13e-05
Planesource	1200	1	M ₁₀₀	old	0.001800	—	2.66e-04	9.43e-04
Sourcebeam	1200	2.5	HFM ₂	new	—	1e-03	1.83e-04	5.52e-04
Sourcebeam	1200	2.5	HFM ₂	old	0.002250	—	2.19e-05	8.27e-04
Sourcebeam	1200	2.5	HFM ₁₀	new	—	1e-03	2.57e-05	8.08e-05
Sourcebeam	1200	2.5	HFM ₁₀	old	0.002250	—	2.49e-05	8.31e-04
Sourcebeam	1200	2.5	HFM ₅₀	new	—	1e-03	7.60e-07	6.42e-07
Sourcebeam	1200	2.5	HFM ₅₀	old	0.002250	—	2.23e-05	8.35e-04
Sourcebeam	1200	2.5	HFM ₁₀₀	new	—	1e-03	1.14e-06	1.01e-06
Sourcebeam	1200	2.5	HFM ₁₀₀	old	0.002250	—	2.23e-05	8.35e-04
Sourcebeam	1200	2.5	PMM ₂	new	—	1e-03	2.43e-04	2.24e-03
Sourcebeam	1200	2.5	PMM ₂	old	0.002250	—	2.21e-05	8.27e-04
Sourcebeam	1200	2.5	PMM ₁₀	new	—	1e-03	5.60e-05	3.17e-04
Sourcebeam	1200	2.5	PMM ₁₀	old	0.002250	—	2.72e-05	8.26e-04
Sourcebeam	1200	2.5	PMM ₅₀	new	—	1e-03	1.59e-07	1.26e-07
Sourcebeam	1200	2.5	PMM ₅₀	old	0.002250	—	2.25e-05	8.26e-04
Sourcebeam	1200	2.5	PMM ₁₀₀	new	—	1e-03	1.74e-07	1.51e-07
Sourcebeam	1200	2.5	PMM ₁₀₀	old	0.002250	—	2.24e-05	8.26e-04
Sourcebeam	1200	2.5	M ₁	new	—	1e-03	3.29e-04	6.00e-03
Sourcebeam	1200	2.5	M ₁	old	0.002250	—	2.21e-05	8.27e-04
Sourcebeam	1200	2.5	M ₁₀	new	—	1e-03	2.21e-07	1.54e-06
Sourcebeam	1200	2.5	M ₁₀	old	0.002250	—	2.95e-05	8.20e-04
Sourcebeam	1200	2.5	M ₅₀	new	—	1e-03	5.35e-07	4.62e-07
Sourcebeam	1200	2.5	M ₅₀	old	0.002250	—	2.28e-05	8.26e-04
Sourcebeam	1200	2.5	M ₁₀₀	new	—	1e-03	1.60e-06	1.55e-06
Sourcebeam	1200	2.5	M ₁₀₀	old	0.002250	—	2.24e-05	8.26e-04

Table A.1: L^1/L^∞ errors compared to reference solution (new scheme with $\tau = 10^{-6}$) for the one-dimensional testcases.

Testcase	I	t_f	Model	Scheme	Δt	τ	E_h^1	E_h^∞
Pointsource	50^3	0.75	M_1	new	—	1e-02	1.35e-04	6.56e-05
Pointsource	50^3	0.75	M_1	old	0.020785	—	1.62e-02	1.24e-02
Pointsource	50^3	0.75	M_2	new	—	1e-02	1.36e-04	1.13e-04
Pointsource	50^3	0.75	M_2	old	0.020785	—	1.56e-02	1.45e-02
Pointsource	50^3	0.75	M_3	new	—	1e-02	1.68e-04	8.16e-05
Pointsource	50^3	0.75	M_3	old	0.020785	—	1.40e-02	9.21e-03
Pointsource	50^3	0.75	M_4	new	—	1e-02	1.74e-04	7.35e-05
Pointsource	50^3	0.75	M_4	old	0.020785	—	1.30e-02	7.88e-03
Pointsource	50^3	0.75	HFM ₆	new	—	1e-02	2.97e-04	5.92e-04
Pointsource	50^3	0.75	HFM ₆	old	0.020785	—	1.27e-02	2.43e-02
Pointsource	50^3	0.75	HFM ₁₈	new	—	1e-02	2.72e-04	2.34e-04
Pointsource	50^3	0.75	HFM ₁₈	old	0.020785	—	1.34e-02	1.48e-02
Pointsource	50^3	0.75	HFM ₆₆	new	—	1e-02	2.86e-04	1.51e-04
Pointsource	50^3	0.75	HFM ₆₆	old	0.020785	—	1.30e-02	8.56e-03
Pointsource	50^3	0.75	PMM ₃₂	new	—	1e-02	4.37e-05	2.84e-05
Pointsource	50^3	0.75	PMM ₃₂	old	0.020785	—	1.31e-02	8.02e-03
Pointsource	50^3	0.75	PMM ₁₂₈	new	—	1e-02	1.24e-05	1.14e-05
Pointsource	50^3	0.75	PMM ₁₂₈	old	0.020785	—	1.30e-02	7.66e-03
Checkerboard	70^3	3.2	M_1	new	—	1e-02	4.50e-05	3.67e-06
Checkerboard	70^3	3.2	M_1	old	0.051962	—	2.10e-02	2.35e-02
Checkerboard	70^3	3.2	M_2	new	—	1e-02	5.10e-05	7.04e-06
Checkerboard	70^3	3.2	M_2	old	0.051962	—	2.36e-02	3.27e-02
Checkerboard	70^3	3.2	M_3	new	—	1e-02	4.54e-05	6.06e-06
Checkerboard	70^3	3.2	M_3	old	0.051962	—	2.43e-02	2.85e-02
Checkerboard	70^3	3.2	PMM ₃₂	new	—	1e-02	4.29e-05	5.52e-06
Checkerboard	70^3	3.2	PMM ₃₂	old	0.051962	—	2.41e-02	2.93e-02
Checkerboard	70^3	3.2	HFM ₆	new	—	1e-02	1.14e-04	1.54e-05
Checkerboard	70^3	3.2	HFM ₆	old	0.051962	—	2.25e-02	2.75e-02
Checkerboard	70^3	3.2	HFM ₁₈	new	—	1e-02	1.19e-04	1.48e-05
Checkerboard	70^3	3.2	HFM ₁₈	old	0.051962	—	2.39e-02	2.95e-02
Shadow	$60 \times 20 \times 15$	20	M_1	new	—	1e-02	1.34e-08	3.84e-09
Shadow	$60 \times 20 \times 15$	20	M_1	old	0.103923	—	4.32e-02	9.14e-03
Shadow	$60 \times 20 \times 15$	20	M_1	old	0.040000	—	1.12e-02	5.28e-03
Shadow	$60 \times 20 \times 15$	20	M_2	new	—	1e-02	5.98e-10	1.25e-10
Shadow	$60 \times 20 \times 15$	20	M_2	old	0.103923	—	3.40e-02	1.06e-02
Shadow	$60 \times 20 \times 15$	20	M_2	old	0.040000	—	8.94e-03	4.42e-03
Shadow	$60 \times 20 \times 15$	20	PMM ₃₂	new	—	1e-02	2.07e-10	7.18e-11
Shadow	$60 \times 20 \times 15$	20	PMM ₃₂	old	0.103923	—	3.30e-02	9.87e-03
Shadow	$60 \times 20 \times 15$	20	PMM ₃₂	old	0.040000	—	8.77e-03	4.39e-03
Shadow	$60 \times 20 \times 15$	20	PMM ₁₂₈	new	—	1e-02	1.29e-10	4.14e-11
Shadow	$60 \times 20 \times 15$	20	PMM ₁₂₈	old	0.103923	—	3.27e-02	9.77e-03
Shadow	$60 \times 20 \times 15$	20	PMM ₁₂₈	old	0.040000	—	8.72e-03	4.39e-03
Shadow	$60 \times 20 \times 15$	20	HFM ₆	new	—	1e-02	3.42e-08	4.82e-09
Shadow	$60 \times 20 \times 15$	20	HFM ₆	old	0.103923	—	2.75e-02	7.22e-03
Shadow	$60 \times 20 \times 15$	20	HFM ₆	old	0.040000	—	7.61e-03	3.55e-03
Shadow	$60 \times 20 \times 15$	20	HFM ₁₈	new	—	1e-02	1.05e-09	2.73e-10
Shadow	$60 \times 20 \times 15$	20	HFM ₁₈	old	0.103923	—	3.04e-02	9.69e-03
Shadow	$60 \times 20 \times 15$	20	HFM ₁₈	old	0.040000	—	8.30e-03	4.31e-03
Shadow	$60 \times 20 \times 15$	20	HFM ₆₆	new	—	1e-02	2.61e-10	9.21e-11
Shadow	$60 \times 20 \times 15$	20	HFM ₆₆	old	0.103923	—	3.29e-02	9.69e-03

Table A.2: L^1/L^∞ errors compared to reference solution (new scheme with $\tau = 10^{-6}$) for the three-dimensional testcases.

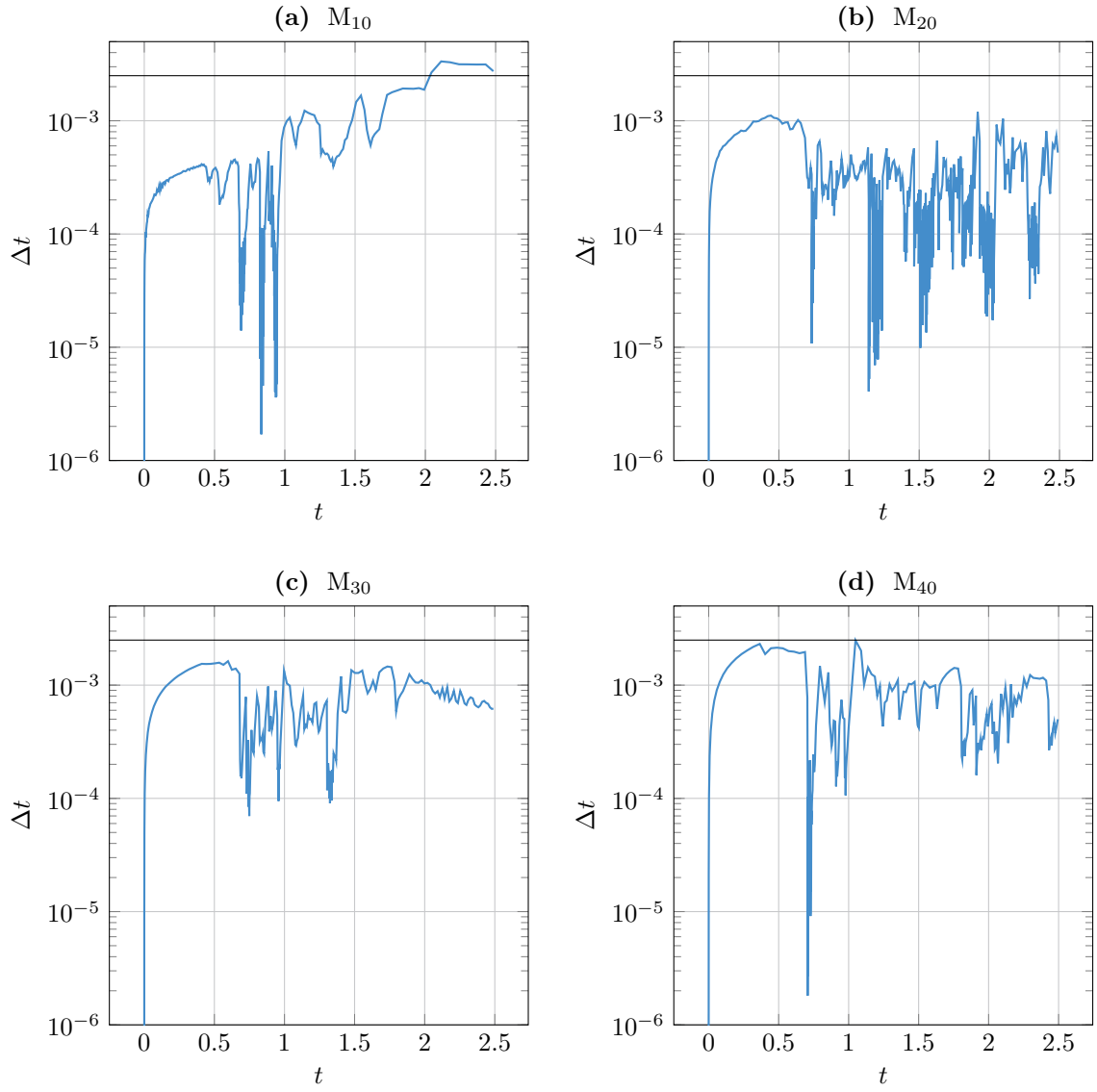


Figure A.3: Timesteps taken in the sourcebeam test case ($I = 1200$, $t_f = 2.5$, $\tau = 10^{-3}$) for different M_N models. The solid line represents the maximum realizability preserving time step Δt_{max} for the standard splitting scheme.

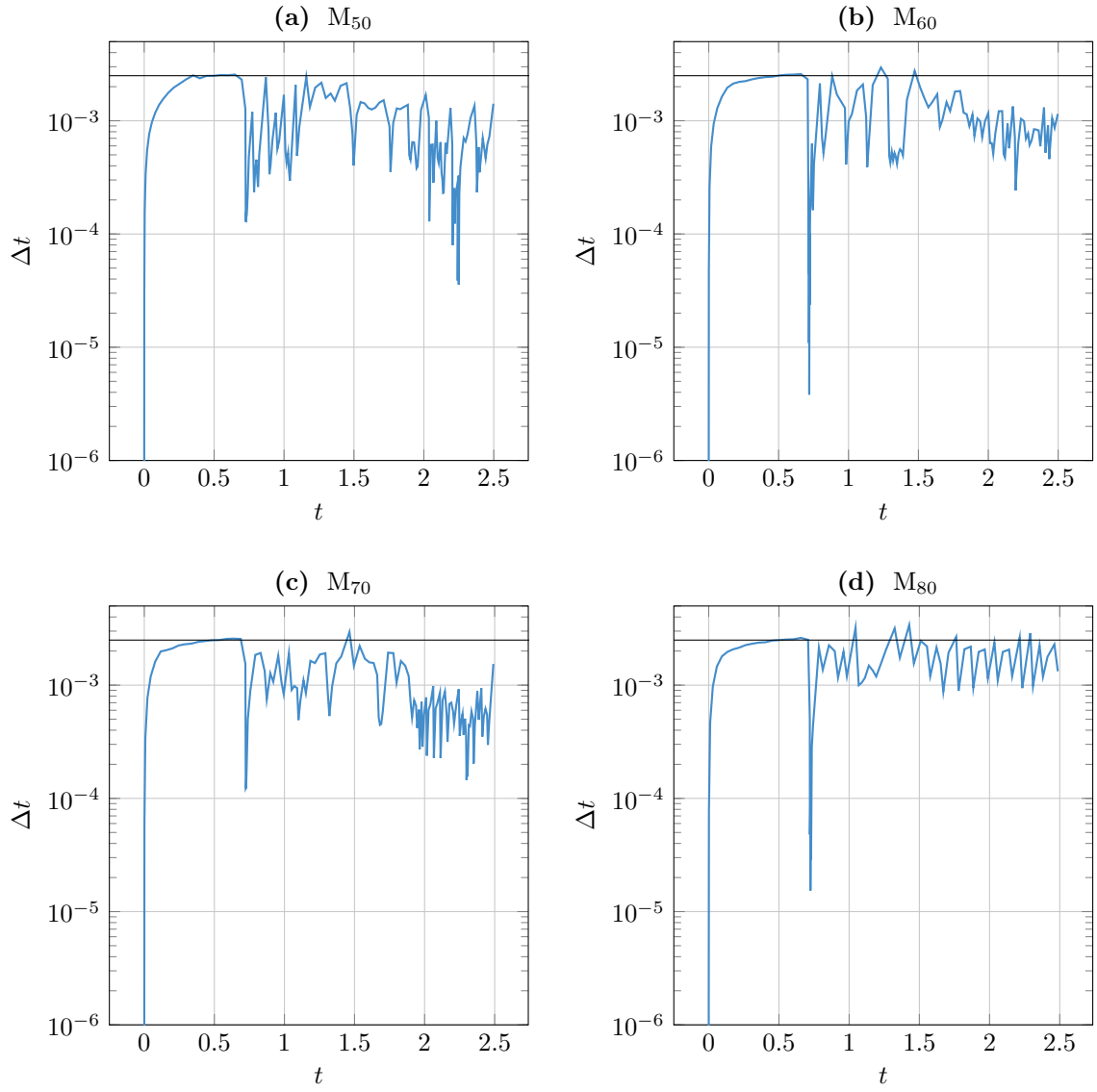


Figure A.4: Timesteps taken in the sourcebeam test case ($I = 1200$, $t_f = 2.5$, $\tau = 10^{-3}$) for different M_N models (continued). The solid line represents the maximum realizability preserving time step Δt_{max} for the standard splitting scheme.

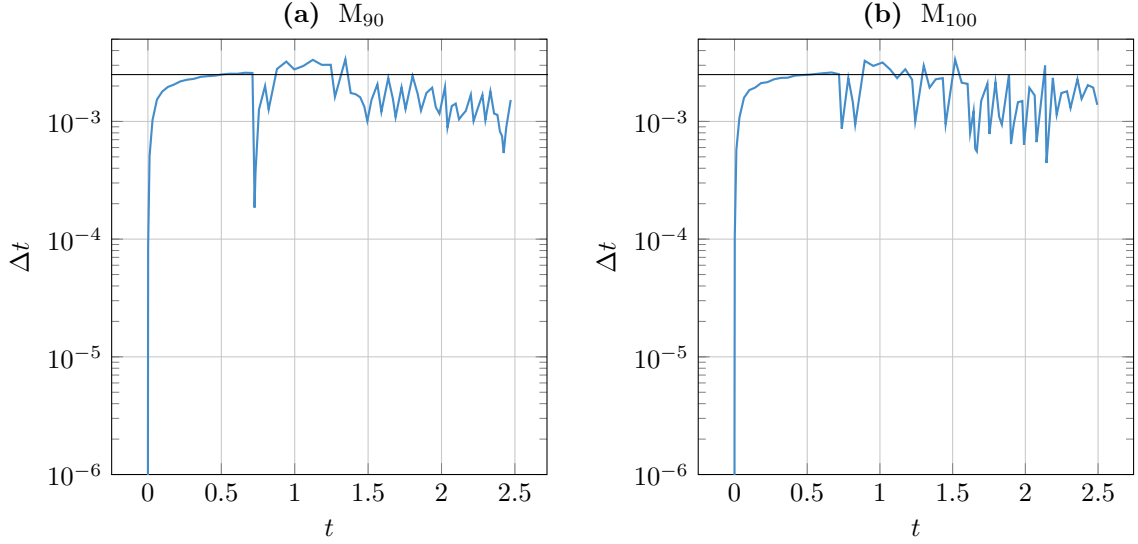


Figure A.5: Timesteps taken in the sourcebeam test case ($I = 1200$, $t_f = 2.5$, $\tau = 10^{-3}$) for different M_N models (continued). The solid line represents the maximum realizability preserving time step Δt_{max} for the standard splitting scheme.

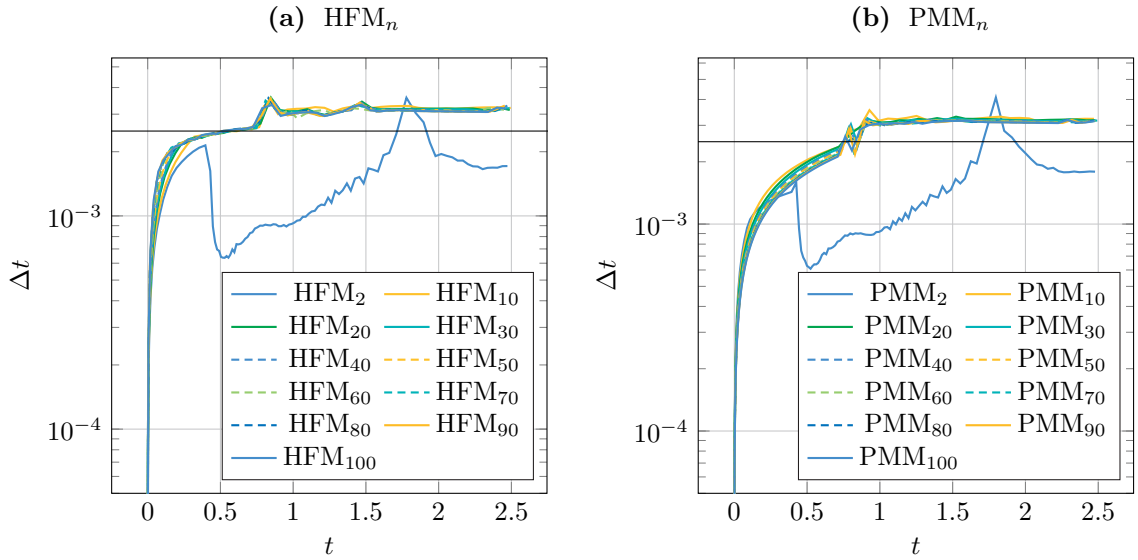


Figure A.6: Timesteps taken in the sourcebeam test case ($I = 1200$, $t_f = 2.5$, $\tau = 10^{-3}$) for HFM_n and PMM_n models. The solid line represents the maximum realizability preserving time step Δt_{max} for the standard splitting scheme.

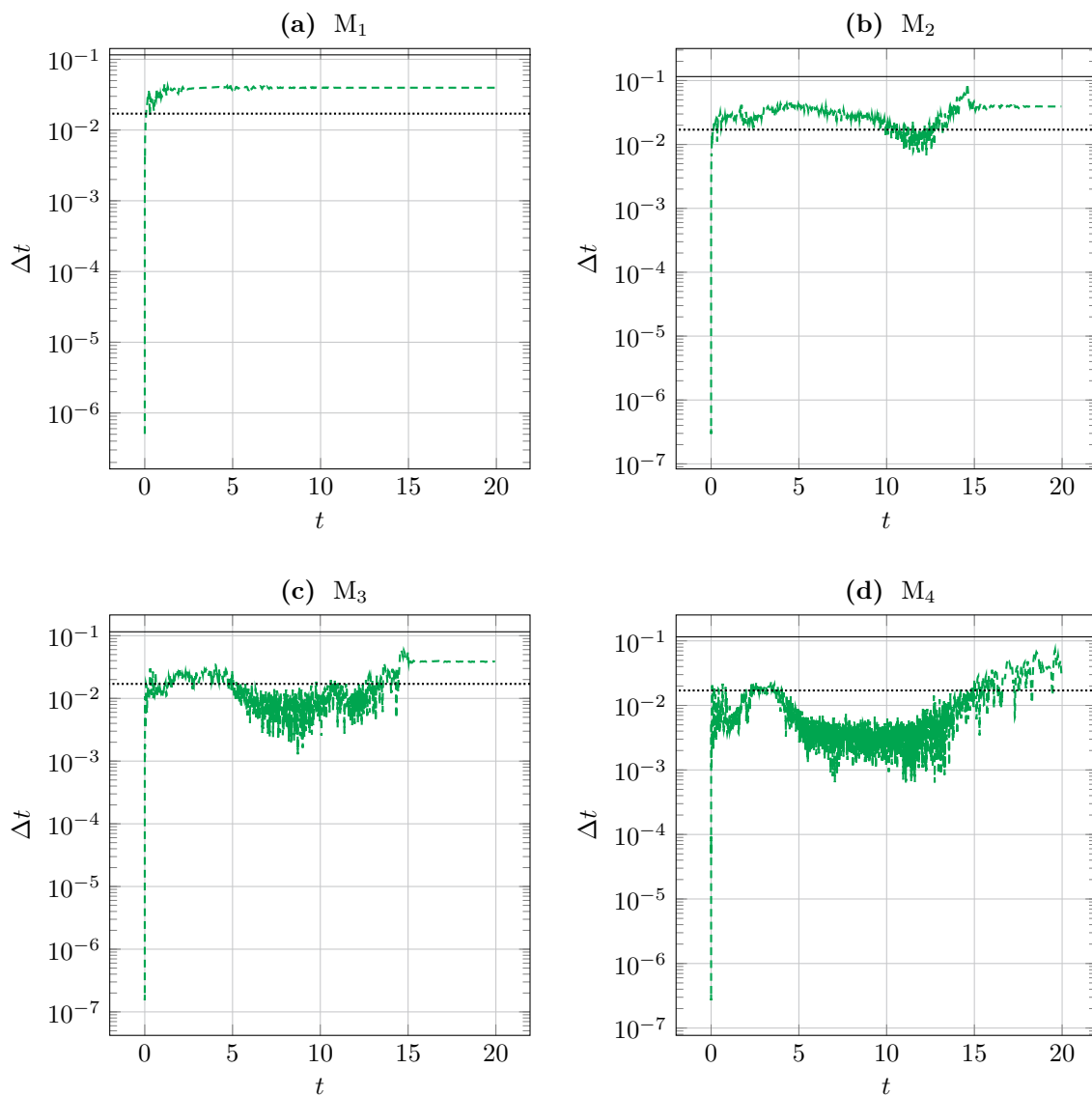


Figure A.7: Timesteps taken in the Shadow test case ($I = 60 \times 20 \times 15$, $t_f = 20$, $\tau = 10^{-2}$) for the M_N models. The solid and dotted horizontal line represent the time step restrictions (3.16) and (3.13), respectively.

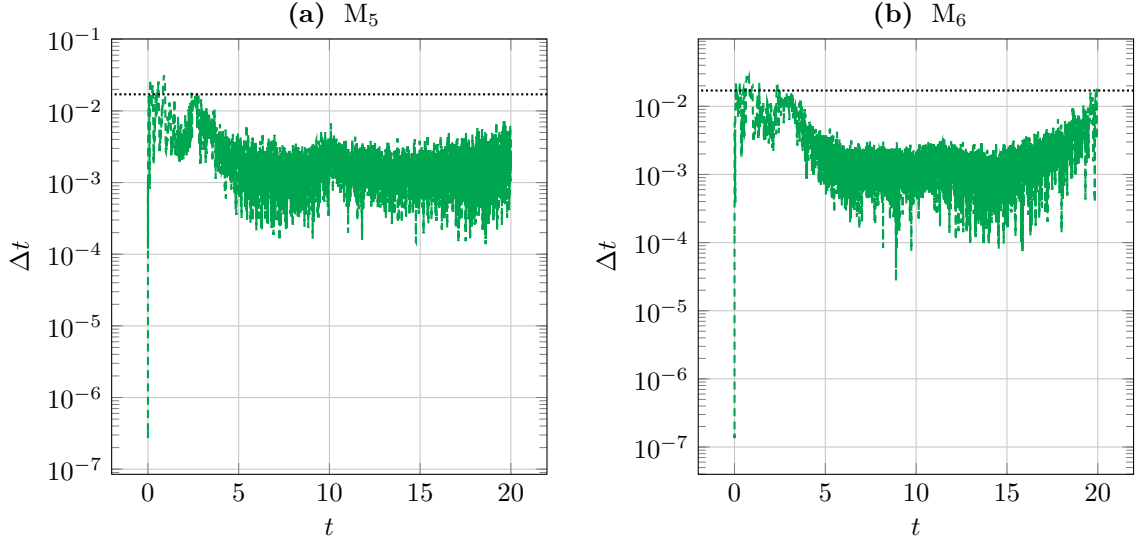


Figure A.8: Timesteps taken in the Shadow test case ($I = 60 \times 20 \times 15$, $t_f = 20$, $\tau = 10^{-2}$) for the M_N models (continued). The solid and dotted horizontal line represent the time step restrictions (3.16) and (3.13), respectively.

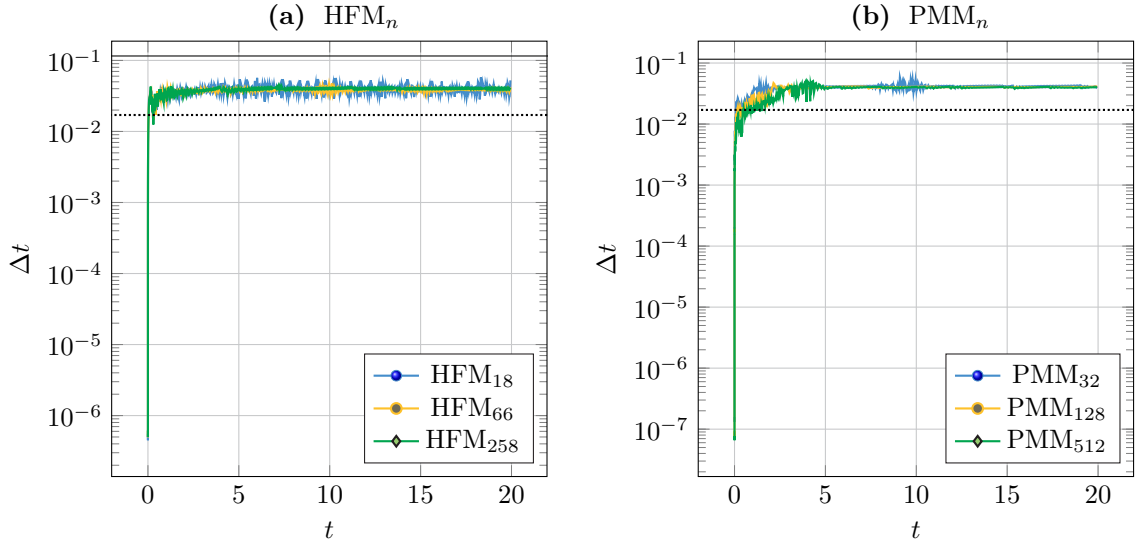


Figure A.9: Timesteps taken in the Shadow test case ($I = 60 \times 20 \times 15$, $t_f = 20$, $\tau = 10^{-2}$) for the HFM_n and PMM_n models. The solid and dotted horizontal line represent the time step restrictions (3.16) and (3.13), respectively.